Energy 346 (2026) 140218

Contents lists available at ScienceDirect

Energy

journal homepage: www.elsevier.com/locate/energy

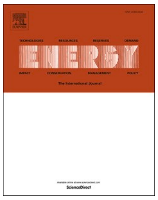

Modeling and experimental validation of self-sensing high-frequency displacement of multi-dimensional discrete magnetostrictive actuator

Chengyuan Li [a], Long Chen [a,b], Hao Zhang [a], Yuchuan Zhu [a,*]

[a] College of Mechanical and Electrical Engineering, Nanjing University of Aeronautics and Astronautics, Nanjing, 210016, Jiangsu, PR China
[b] College of Engineering, Nanjing Agricultural University, Nanjing, 210031, Jiangsu, PR China

ARTICLE INFO

Keywords:
Multi-dimensional discrete magnetostrictive actuator
Dual spool fuel valve
Self-sensing high-frequency displacement
Theoretical model
Surrogate model
Closed-loop control experiment

ABSTRACT

A dual spool fuel valve has been developed for active control of combustion oscillations in aeroengines. The inner spool, directly driven by a multi-dimensional discrete magnetostrictive actuator (MDMA), regulates high-frequency fuel flow to meet the demands of active control system. Precise control of high-frequency fuel flow is critical for effective active control, necessitating accurate monitoring of the inner spool position. Traditional contact-based measurements, which rely on displacement sensors, are limited by integration complexity and intricate structural requirements. In contrast, displacement self-sensing methods for the MDMA offer a novel solution for monitoring the inner spool position. Therefore, this study presented a displacement self-sensing strategy employing four induction coils and developed a theoretical model based on the energy transfer process. However, the theoretical model exhibited low computational efficiency, and the induced current lagged behind the displacement, making it unsuitable for real-time high-frequency displacement calculation. To address this limitation, a real-time displacement self-sensing surrogate model (RDSSM) combining a two-layer multilayer perceptron network with a discrete wavelet transform algorithm was proposed. Experiments showed that the theoretical model had an average modeling error of 5.48 %, while the RDSSM achieved an error of 3.63 %. Furthermore, the closed-loop control experiments revealed an average relative error of 3.76 % between feedback displacement derived from the RDSSM and direct measurements, validating that the RDSSM can effectively replace traditional displacement sensors, enabling accurate self-sensing, feedback, and control of the inner spool position.

1. Introduction

In civil aviation, lean premixed pre-vaporized combustion technology is widely employed to improve combustion efficiency and reduce pollutant emissions [1,2]. However, this technology is susceptible to inducing combustion oscillations in aeroengines [3], which significantly compromise the safety and reliability of propulsion system operations [4,5]. Empirical studies have indicated that the active control methods, based on high-frequency fuel flow regulation, are the most effective and practical means of suppressing combustion oscillations [6]. However, these methods require the fuel valve capable of regulating the high-frequency and large-amplitude fuel flow, while also maintaining a compact design and withstanding high-temperature environments. Conventional electromagnetic-driven fuel valves are insufficient to meet these stringent requirements [7,8].

The magnetostrictive actuators are distinguished by their simple design, high energy density, and rapid frequency response, making them widely used in applications such as energy conversion [9], active vibration suppression [10], and fluid control [11], especially in high-frequency fluid control scenarios [12]. Notably, a high-frequency fuel valve based on a magnetostrictive actuator had been implemented in an active control ground test system of combustion oscillations [13]. However, the overall length of this fuel valve, up to 45.7 cm, presented significant challenges for its practical integration into aeroengines.

In our previous study, a dual spool fuel valve (DSFV) based on a multi-dimensional discrete magnetostrictive actuator (MDMA) was designed and developed [14,15]. The valve featured both the inner and outer spools capable of axial displacement, which collectively regulate the valve opening. The inner spool, actuated by the MDMA, enabled modulation of high-frequency, small-amplitude flow to address the

---

[*] Corresponding author. College of Mechanical and Electrical Engineering, Nanjing University of Aeronautics and Astronautics, No. 29, Yudao street, Qinhuai District, Nanjing, 210016, PR China.
E-mail address: meeyczhu@nuaa.edu.cn (Y. Zhu).

https://doi.org/10.1016/j.energy.2026.140218
Received 30 October 2025; Received in revised form 25 December 2025; Accepted 26 January 2026

active control requirements of combustion oscillations. In contrast, the outer spool, driven by a voice coil motor (VCM), generated low-frequency, large-amplitude flow to satisfy the fuel supply demands of conventional aeroengine operation. With a compact length of 13.9 cm of the DSFV, experimental evaluations demonstrated that the inner spool achieved a displacement of 101 μm, a frequency bandwidth exceeding 1000 Hz, and a displacement attenuation of less than 13 % at an ambient temperature of 120 °C [16]. Furthermore, the semi-physical experiments, based on the DSFV prototype and high-frequency combustion oscillation model, indicated that the DSFV could effectively suppress multimodal combustion oscillations under different operating conditions [17]. These findings highlighted the significant potential of the DSFV for implementation in active control systems of combustion oscillations in aeroengines.

To achieve high-frequency and high-precision flow control of the DSFV, real-time monitoring of the inner spool position is essential. Traditional methods for measuring spool position primarily rely on displacement sensors; however, these techniques are limited by integration complexity and intricate structural requirements. Magnetostrictive materials, characterized by their magnetostrictive and inverse magnetostrictive effects, offer promising self-sensing capabilities for measuring parameters such as displacement, output force, and stress. Currently, extensive research has been conducted in this area, with detailed information summarized in Table 1.

In the investigation of parameter self-sensing for magnetostrictive actuators, existing techniques predominantly rely on self-sensing signals obtained from induction or excitation coils, followed by off-line parameters reconstruction based on theoretical models. Although these methods achieved high reconstruction accuracy, their applicability was largely limited to quasi-static or low-frequency scenarios and had not been effectively extended to high-frequency applications. Notably, the dominant frequency of combustion oscillations in aeroengines typically exceeds 500 Hz [28], requiring fuel valves to regulate fuel flow at frequencies above this threshold. Therefore, achieving high-frequency displacement self-sensing of the inner spool is crucial to ensure the functional integration, compactness, and reliable performance of the DSFV.

The theoretical model of self-sensing displacement, based on the energy transfer process, is characterized by significant model complexity and limited computational efficiency, which impedes its ability to satisfy the real-time requirement of high-frequency displacement monitoring. Additionally, the self-sensing signals produced by the induction coils exhibit a phase lag relative to the displacement signal, restricting the application of the theoretical model to off-line analyses and preventing its use in real-time on-line computations. To address these limitations, surrogate modeling approaches have been widely adopted as alternative approaches for representing complex systems due to their improved computational efficiency and flexible data-driven characteristic. Common modeling techniques include linear regression [29,30], random forests [31,32], support vector machines [33,34], Gaussian processes [35,36], and neural networks [37–39]. Among these, linear regression offers limited fitting accuracy and fails to adequately capture nonlinear dynamics. Conversely, methods such as random forests, support vector machines, Gaussian processes, and deep neural networks provide superior fitting accuracy but suffer from low computational efficiency, which similarly presents challenges in meeting the real-time requirements of high-frequency application scenarios. In contrast, shallow neural networks strike a favorable balance between computational efficiency and fitting accuracy, making them the preferred approach for developing real-time predictive model of self-sensing displacement.

Therefore, to enable non-contact high-frequency displacement measurement of the inner spool within the DSFV, this study proposed a self-sensing displacement approach using four sets of induction coils arranged axially within the MDMA. Firstly, a theoretical model, based on the energy transfer process, was developed to explain the fundamental principle of self-sensing displacement. Secondly, to address the limitations of the theoretical model in high-frequency displacement real-time monitoring, a real-time displacement self-sensing surrogate model (RDSSM) was proposed, employing a two-layer multilayer perceptron (MLP) network. The proposed RDSSM predicted the self-sensing displacement by the sampled data from four distinct sets of inductions coils over five consecutive time intervals. Additionally, the Discrete Wavelet Transform (DWT) algorithm was applied to extract both approximation and detail coefficients from the input current sequences, thereby improving the accuracy of RDSSM. Finally, high-frequency displacement closed-loop control experiments on the inner spool were conducted to validate that the RDSSM can effectively replace traditional displacement sensors, enabling accurate self-sensing, feedback, and control of the inner spool position.

The remainder of this paper is structured as follows: Section 2 provides the structural introduction of the DSFV and MDMA, along with a detailed analysis of displacement formation and self-sensing mechanisms of the MDMA. Section 3 explains the theoretical model and RDSSM of the self-sensing displacement. Section 4 presents the physical prototype of the DSFV along with the experimental platform, where experiments were conducted to evaluate the modeling accuracy of the theoretical model and the RDSSM. In Section 5, the closed-loop control experiments were conducted to validate the accuracy and effectiveness of the RDSSM in closed-loop control applications. Finally, Section 6 provides the conclusion.

2. The structure and working principle of the DSFV and MDMA

2.1. *The structure of the DSFV and MDMA*

Fig. 1 illustrates the structural schematic of the DSFV, which primarily consists of five components: the MDMA, the inner spool, the outer spool, the VCM, and the valve body. The inner and outer spools are radially nested within the fuel valve and can move axially to collectively regulate the valve opening, thereby regulating the outlet flow. Specifically, the inner spool is directly driven by the MDMA to generate high-frequency, small-amplitude flow to address the active control requirements of combustion oscillations. In contrast, the outer spool is

Table 1
Summary of research on self-sensing magnetostrictive actuators.

Time	Researcher	Self-sensing device	Self-sensing parameter	Self-sensing model	On/off line	Frequency	Precision
2024	Yang [18]	Induction coils	Force	Theoretical model	Off	10Hz	92.6 %
2024	Yang [19]	Induction coils	Displacement	Network model	On	10Hz	97.1 %
2024	Wang [20]	Excitation coils	Displacement	Theoretical model	Off	5Hz	84.2 %
2022	Yang [21]	Induction coils	Displacement	Theoretical model	Off	0.5Hz	95 %
2019	Valerio [22]	Induction coils	Stress	–	On	Quasi-static	88 %
2017	Yang [23]	Excitation coils	Stress	Theoretical model	Off	0.5Hz	–
2014	Yan [24]	Excitation coils	Vibration	Theoretical model	Off	–	–
2014	Yan [25]	Excitation coils	Stress	Theoretical model	Off	–	80 %
2013	Sun [26]	Excitation coils	Displacement	–	On	–	–
2007	Kuhnen [27]	Hall sensor	Displacement	–	On	–	85.56 %

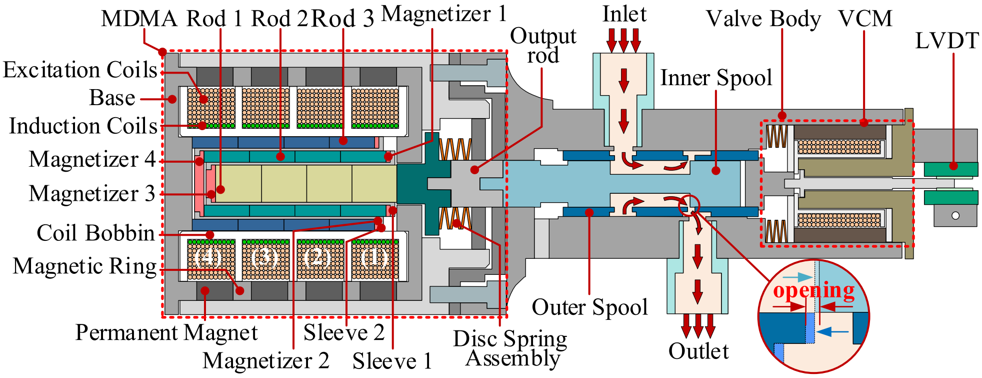

Fig. 1. The structural schematic of the DSFV.

directly driven by the VCM to generate low-frequency, large-amplitude flow to satisfy the fuel supply demands of conventional aeroengine operation.

As illustrated in Fig. 1, the primary structure of the MDMA consists of three distinct components. The first component comprises the Multidimensional Discrete Magnetostrictive Stack (MDMS), which comprises three magnetostrictive rods, two sleeves, and four magnetizers. As illustrated in Fig. 2, this configuration enables axial displacement transmission from the three rods through the sleeves, thereby facilitating the amplification of the MDMA's displacement. The second component is the Discrete Electromagnetic Excitation Mechanism (DEEM), which includes four sets of excitation coils, four sets of induction coils, a coil frame, four permanent magnets, and three magnetic rings. By axially segmenting the excitation coils into four separate groups, the impedance of the coils is reduced, thereby effectively enhancing the frequency response of the MDMA. Additionally, the four sets of induction coils serve the purpose of self-sensing displacement. The third component is the Preload Application Mechanism (PAM), comprising a disc spring assembly, an output rod, and a pre-tightening end cover. The PAM supplies the necessary prestress to ensure the proper operation of the MDMA.

2.2. *The displacement formation and self-sensing mechanisms of the MDMA*

Fig. 3 illustrates the displacement formation and self-sensing mechanisms of the MDMA. Among these, the red arrows indicate the sequence of energy transfer and displacement formation within the MDMA upon application of the excitation current. Initially, the signal generator supplies driving voltage signals to four power amplifiers, which then produce excitation currents in four sets of excitation coils. These excitation currents generate magnetic fields that interact with the magnetic fields from the permanent magnets, resulting in a specific magnetic field distribution within the MDMS. Under the influence of this combined magnetic field, the three magnetostrictive rods are magnetized, causing deflection of the internal magnetic domains and generating magnetostrictive strain and force. Ultimately, the multi-body dynamic system, comprising the MDMS and PAM, converts the magnetostrictive force into the output displacement of the MDMA.

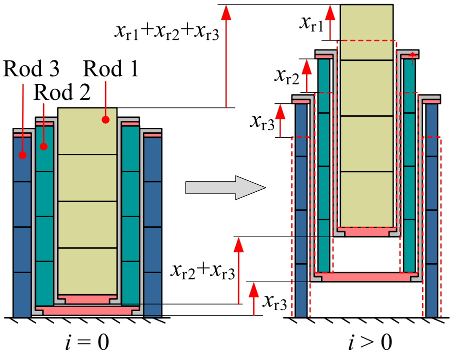

Fig. 2. The displacement amplification principle of the MDMS. In which, x_{r1}, x_{r2} and x_{r3} represent the displacement of Rod 1, Rod 2 and Rod 3, respectively.

In Fig. 3, the blue arrows illustrate the displacement self-sensing mechanism and the associated computational procedure. Variations in the excitation current cause corresponding changes in both the direction and magnitude of the internal magnetic field within the MDMS. According to Faraday's law of electromagnetic induction, these changes induce currents in the four sets of closed induction coils surrounding the MDMS. Through measuring these induced currents, the magnetic induction intensity of the three magnetostrictive rods can be determined. Utilizing the mathematical relationships among magnetization, magnetic induction intensity, and magnetic field intensity, the magnetization of the three rods is then calculated. Subsequently, by establishing a mathematical model relating magnetization to magnetostrictive force, the output magnetostrictive force of the rods is obtained. Finally, the displacement of MDMA is derived by applying a multibody mechanical dynamic model that characterizes the relationship between force and motion, thereby formulating the mathematical model of self-sensing displacement.

3. Self-sensing displacement model

This section establishes the theoretical model and RDSSM of the self-sensing displacement. Firstly, the theoretical model based on the energy transfer process is described in detail. Secondly, it introduces the RDSSM based on the DWT algorithm and a two-layer MLP network. The discussion covers the architecture and operational mechanism of RDSSM, and the theoretical foundations of both the DWT algorithm and the MLP network.

3.1. *Theoretical model*

The equivalent magnetic circuit of the MDMA is shown in Fig. 4. As illustrated, the magnetic flux within Induction Coil 1 encompasses that of the output rod (ϕ_8), the magnetizers (ϕ_9, ϕ_{10}), the radial leakage flux (ϕ_4, ϕ_5), the air gap (ϕ_9, ϕ_{10}), and the magnetostrictive rods (ϕ_1, ϕ_2, ϕ_3). Meanwhile, the magnetic flux within Induction Coil 4 encompasses that of the base (ϕ_{13}), the magnetizers (ϕ_{11}, ϕ_{12}), the radial leakage flux (ϕ_6, ϕ_7), the air gap (ϕ_{11}, ϕ_{12}), and the magnetostrictive rods (ϕ_1, ϕ_2, ϕ_3). In contrast, the magnetic flux within Induction Coils 2 and 3 only encompasses that of the magnetostrictive rods (ϕ_1, ϕ_2, ϕ_3).

According to the displacement formulation process of the MDMA,

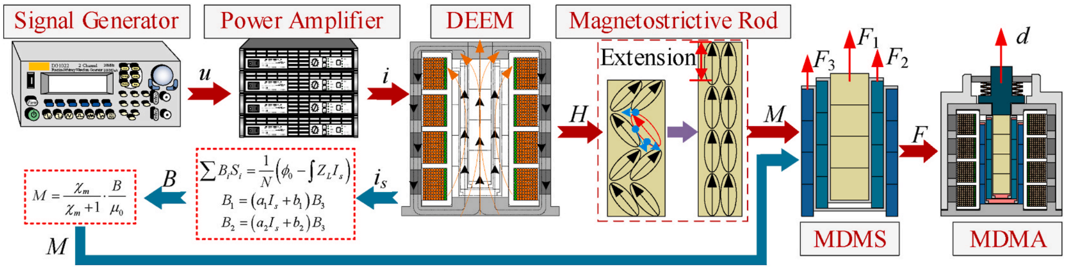

Fig. 3. The schematic of the displacement formation and self-sensing mechanisms of the MDMA.

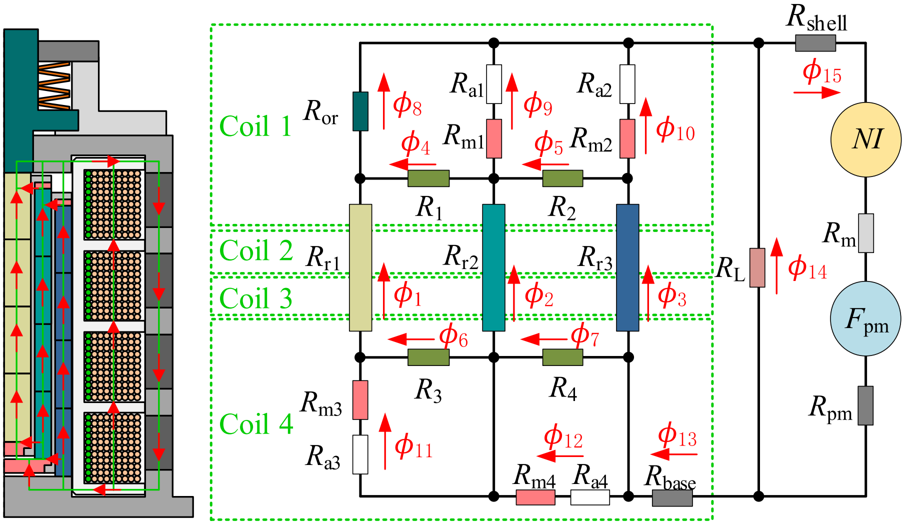

Fig. 4. The schematic of equivalent magnetic circuit of the MDMA.

illustrated in Section 2.2, the output displacement of the MDMA primarily results from the magnetization and subsequent deformation of the magnetostrictive rods within the magnetic field. In order to accurately quantify the relationship between the induced current and the output displacement, it is essential to calculate only the magnetic flux associated with the magnetostrictive rods, thereby avoiding errors caused by magnetic flux contributions from other components. Therefore, the induced current of Induction Coils 2 was chosen as the input parameters of the theoretical model, which consisted of three components: the magnetization model, the magnetostrictive force model, and the multibody mechanical dynamic model.

3.1.1. *Magnetization model*

According to Faraday's law of electromagnetic induction, the induced current, labeled as i_s, generated within the closed coil subjected to an alternating magnetic field can be expressed as:

$$i_s = \frac{u_s}{Z_L} = -\frac{N}{Z_L}\frac{d\phi_s}{dt} \tag{1}$$

Where ϕ_s represents the magnetic flux within the coil; u_s, N and Z_L represent the induced voltage, the turns and the impedance of the coil, respectively. Z_L can be calculated by:

$$Z_L = \sqrt{R_L^2 + X_L^2} = \sqrt{R_L^2 + 4\pi^2 f^2 L^2} \tag{2}$$

Where R_L, L and X_L represent the resistance, the inductor and the inductive impedance of the coil, respectively; f represents the frequency of the alternating magnetic field.

As illustrated in Fig. 4, the magnetic flux within the induction coil 2 represents the sum of the magnetic fluxes of the three magnetostrictive rods. However, due to the complex configuration of the magnetic circuit within the MDMS, the magnetic flux and magnetic induction intensity associated with each of the three rods vary. Consequently, based on equation (1), the following expression can be derived:

$$\phi_s = \phi_1 + \phi_2 + \phi_3 = B_1 S_1 + B_2 S_2 + B_3 S_3 = \phi_0 - \frac{1}{N}\int Z_L i_s \tag{3}$$

Where B_1, B_2 and B_3 represent the magnetic induction intensity of Rod 1, Rod 2 and Rod 3, respectively; S_1, S_2 and S_3 represent the cross-sectional area of Rod 1, Rod 2 and Rod 3, respectively; ϕ_0 represents the initial magnetic flux within the Induction Coil 2.

When the excitation current i varies sinusoidally as $i = i_m \sin\omega t$, the excitation magnetic field H and the magnetic flux ϕ_s within the induction coil also vary sinusoidally, denoted as $H = H_m \sin\omega t$ and $\phi_s = \phi_m \sin\omega t$, respectively. Under these conditions, the induced voltage in the induction coil is represented as $u_s = -N\phi_m\ \omega\cos\omega t$, indicating that the phase of the induced voltage lags behind the phase of the magnetic flux by an angle $\pi/2$. Furthermore, the impedance angle of the induction coil is given by $\varphi = \arctan\ (X_L/R_L)$, which means that the phase of the induced current lags behind that of the induced voltage by an angle φ. Consequently, the phase of the induced current lags behind that of the magnetic flux by an angle $(\pi/2+\varphi)$. Therefore, the magnetic flux ϕ_s within the coil at time t_0 is expressed as:

$$\begin{cases} \phi_s(t_0) = B_1(t_0)S_1 + B_2(t_0)S_2 + B_3(t_0)S_3 = \phi_0 - \dfrac{Z_L}{N}\displaystyle\int i_s(t_1) \\ t_1 = t_0 + 0.25T + \varphi T/2\pi \end{cases} \tag{4}$$

Where T represent the period of the excitation current, with a value of $1/f$.

In order to obtain the magnetic induction intensity distribution characteristics of three magnetostrictive rods under different excitation currents, the steady-state simulations were carried out on the two-dimensional axisymmetric model of MDMA utilizing the Magnetic Fields module within the AC/DC interface of the COMSOL Multiphysics software. The simulation model primarily comprised the MDMA model alongside an air domain measuring 100 mm in length and 150 mm in width. A globally refined triangular mesh was automatically constructed based on predefined meshing parameters, which are detailed in Table 2. The magnetic field simulation model and mesh generation results are illustrated in Fig. 5.

The boundary conditions employed in the magnetic field simulation model primarily encompass axisymmetric boundaries, magnetic insulation boundaries, the application of Ampere's law, and coil modeling. Specifically, the axisymmetric and magnetic insulation boundaries are illustrated in Fig. 5(a). The four excitation coil regions were set as coil models, each incorporating a uniform multi-turn current excitation source. The coils were characterized by 168 turns and a wire diameter of 0.6 mm. The magnetization and dielectric properties were modeled through relative permeability and relative permittivity, respectively. For the remaining regions, the computational models were set by Ampere's law, with conductivity and relative permittivity parameters defining the conduction and dielectric models, respectively. Notably, the magnetization models of the magnetostrictive rods and magnetizers were set by their respective B-H characteristic curves, whereas the permanent magnets were characterized magnetically by their remanent magnetic flux density, specified as 0.52 in the axial direction. Other regions utilized relative permeability to describe their magnetization behavior. Detailed material and parameter definitions for each region are provided in Table 3. Additionally, the B-H characteristic curves corresponding to the magnetostrictive and DT4C material, as supplied by the raw material manufacturer, are presented in Fig. 5(c) and (d), respectively.

The results are presented in Fig. 6. Specifically, subfigures (a) to (f) show the cloud maps of the magnetic induction intensity within the MDMA, while subfigure (g) illustrates the ratios of the magnetic induction intensity of Rod 1 and Rod 2 to that of Rod 3.

The results indicated that variations of the excitation current caused corresponding changes in the magnetic induction intensity of the three magnetostrictive rods, and the ratios of the magnetic induction intensity of Rod 1 and Rod 2 to that of Rod 3 showed minor fluctuations. Additionally, the induced current exhibited a functional relationship with respect to the excitation current, denoted as $i_s = f(i)$. Consequently, the distribution ratios of B_1, B_2 and B_3 under different excitation magnetic fields was described by a first-order polynomial functions of the induced current, as expressed:

$$\begin{cases} B_1 = (\alpha_1 i_s + \beta_1) B_3 \\ B_2 = (\alpha_2 i_s + \beta_2) B_3 \end{cases} \tag{5}$$

Where α_1 and α_2 are the coefficients of linear term; β_1 and β_2 are the coefficients of constant term.

When the magnetostrictive rod is subjected to magnetization by an external magnetic field, the resulting magnetic induction intensity is influenced by both the external magnetic field intensity and the intrinsic magnetization of the rod. The magnetic induction intensity can be expressed by the following relation:

$$B = \mu_0 (H + M) = \mu_0 \left(\frac{M}{\chi_m} + M \right) \tag{6}$$

Where μ_0 represents the vacuum permeability; χ_m represents the magnetic susceptibility of the magnetostrictive rod. Therefore, the magnetization of the rod can be calculated as follows:

$$M = \frac{\chi_m}{\chi_m + 1} \cdot \frac{B}{\mu_0} \tag{7}$$

Table 2
The definitions of mesh parameters for magnetic field simulation model.

Parameter	Value
Maximum unit size (mm)	1.5
Minimum unit size (mm)	0.003
Maximum unit growth rate	5
Curvature factor	0.2
Resolution in narrow areas	1

3.1.2. *Magnetostrictive force model*

The prestress and magnetic field intensity significantly influence the magnetization and deformation behavior of magnetostrictive rod, serving as the primary factors governing magnetostrictive force. The magnetostrictive strain of the rod, which depends on the applied prestress, can be determined as follows [40]:

$$\begin{cases} \lambda = \left(1 + \frac{1}{2}\tanh\frac{2\sigma_p}{\sigma_s}\right)\lambda_s \frac{M^2}{M_s^2}, \sigma_p \le \sigma_s \\ \lambda = \left(1 - \frac{\sigma_p - \sigma_s}{\sigma_{max}}\right)\left(1 + \frac{1}{2}\tanh\frac{2\sigma_p}{\sigma_s}\right)\lambda_s \frac{M^2}{M_s^2}, \sigma_p > \sigma_s \end{cases} \tag{8}$$

Where M_s and λ_s represent the saturation magnetization and the saturation magnetostrictive strain coefficient of the rod, respectively; σ_p, σ_s and σ_{max} represent the actual prestress, the optimal prestress, and the maximum magnetostrictive stress of the rod, respectively, and can be calculated as follows:

$$\begin{cases} \sigma_p = F_p / S \\ \sigma_s = \lambda_s E_G / 2 \\ \sigma_{max} = 3\lambda_s E_G / 2 \end{cases} \tag{9}$$

Where F_p, E_G and S represent the preload, the elastic modulus, and the cross-sectional area of the magnetostrictive rod.

The magnetostrictive force F generated by the rod is ultimately calculated as follows:

$$F = \lambda E_G S \tag{10}$$

3.1.3. *Multibody mechanical dynamic model*

As illustrated in Fig. 7, the multibody mechanical dynamic system, consisting of three magnetostrictive rods, two sleeves, four magnetizers, an output rod, and a disc spring assembly, converts the deformation and force generated by the three rods into the displacement of the MDMA. Each rod must overcome not only its intrinsic mass, stiffness, and damping, but also those of the equivalent load acting along the direction of displacement.

The dynamic equations of the three rods and the displacement of MDMA are as follows:

$$\begin{cases} \left(\frac{m_{r1}}{3} + m_{eq1}\right)\ddot{x}_{r1} + (c_{r1} + c_{eq1})\dot{x}_{r1} + (k_{r1} + k_{eq1})x_{r1} = F_{r1} \\ \left(\frac{m_{r2}}{3} + m_{eq2}\right)\ddot{x}_{r2} + (c_{r2} + c_{eq2})\dot{x}_{r2} + (k_{r2} + k_{eq2})x_{r2} = F_{r2} \\ \left(\frac{m_{r3}}{3} + m_{eq3}\right)\ddot{x}_{r3} + (c_{r3} + c_{eq3})\dot{x}_{r3} + (k_{r3} + k_{eq3})x_{r3} = F_{r3} \\ d = x_{r1} + x_{r2} + x_{r3} \end{cases} \tag{11}$$

Where d represent the displacement of MDMA; m_{r1}, m_{r2} and m_{r3} represent the mass of Rod 1, Rod 2 and Rod 3, respectively; c_{r1}, c_{r2} and c_{r3} represent the damping of Rod 1, Rod 2 and Rod 3, respectively; k_{r1}, k_{r2} and k_{r3} represent the stiffness of Rod 1, Rod 2 and Rod 3, respectively; F_{r1}, F_{r2} and F_{r3} represent the magnetostrictive force of Rod 1, Rod 2 and Rod 3, respectively; m_{eq1}, m_{eq2}, m_{eq3}, c_{eq1}, c_{eq2}, c_{eq3}, k_{eq1}, k_{eq2} and k_{eq3} represent the mass, damping and stiffness of the equivalent load of Rod 1, Rod 2 and Rod 3, respectively, and can be calculated as follows [40]:

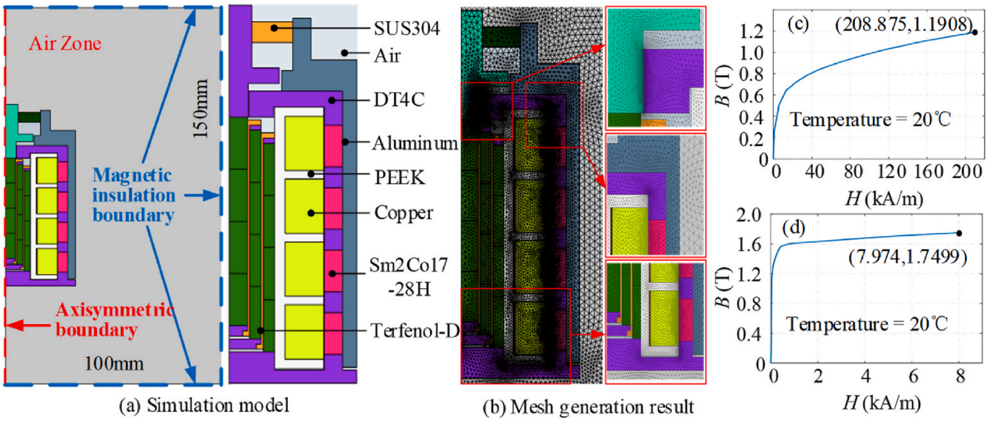

(a) Simulation model (b) Mesh generation result

Fig. 5. The magnetic field simulation model, mesh generation results and the B-H characteristic curves of magnetostrictive and DT4C materials.

Table 3
The material and parameter definitions for each region of the magnetic field simulation model.

Material	Region	Relative permeability	Electrical conductivity (S/m)	Relative dielectric constant
Terfenol-D	Magnetostrictive Rods	–	1.667×10^6	1
DT4C	Magnetizers, Magnetic Rings, Magnetic Cover, Base, Output Rod	–	1.03×10^7	1
SUS304	Sleeves, Pre-tightening End Cover	1.3	1.739×10^6	1
PEEK	Coil Bobbin	1	0	4
Copper	Coils	1	5.998×10^7	1
Sm2Co17-28H	Permanent Magnets	–	0.8	1
Aluminum	Outer Shell	1	3.774×10^7	1

$$\begin{cases} m_{\mathrm{eq1}} = m_{\mathrm{load}} \\ m_{\mathrm{eq2}} = m_{\mathrm{m1}} + m_{\mathrm{t1}} + m_{\mathrm{m3}} + m_{\mathrm{r1}} + m_{\mathrm{load}} \\ m_{\mathrm{eq3}} = m_{\mathrm{m2}} + m_{\mathrm{t2}} + m_{\mathrm{m4}} + m_{\mathrm{r2}} + m_{\mathrm{m1}} + m_{\mathrm{t1}} + m_{\mathrm{m3}} + m_{\mathrm{r1}} + m_{\mathrm{load}} \\ c_{\mathrm{eq1}} = \left(\dfrac{1}{c_{\mathrm{load}}} + \dfrac{1}{c_{\mathrm{d}}}\right)^{-1} \\ c_{\mathrm{eq2}} = \left(\dfrac{1}{c_{\mathrm{m1}}} + \dfrac{1}{c_{\mathrm{t1}}} + \dfrac{1}{c_{\mathrm{m3}}} + \dfrac{1}{c_{\mathrm{r1}}} + \dfrac{1}{c_{\mathrm{load}}} + \dfrac{1}{c_{\mathrm{d}}}\right)^{-1} \\ c_{\mathrm{eq3}} = \left(\dfrac{1}{c_{\mathrm{m2}}} + \dfrac{1}{c_{\mathrm{t2}}} + \dfrac{1}{c_{\mathrm{m4}}} + \dfrac{1}{c_{\mathrm{r2}}} + \dfrac{1}{c_{\mathrm{m1}}} + \dfrac{1}{c_{\mathrm{t1}}} + \dfrac{1}{c_{\mathrm{m3}}} + \dfrac{1}{c_{\mathrm{r1}}} + \dfrac{1}{c_{\mathrm{load}}} + \dfrac{1}{c_{\mathrm{d}}}\right)^{-1} \\ k_{\mathrm{eq1}} = \left(\dfrac{1}{k_{\mathrm{load}}} + \dfrac{1}{k_{\mathrm{d}}}\right)^{-1} \\ k_{\mathrm{eq2}} = \left(\dfrac{1}{k_{\mathrm{m1}}} + \dfrac{1}{k_{\mathrm{t1}}} + \dfrac{1}{k_{\mathrm{m3}}} + \dfrac{1}{k_{\mathrm{r1}}} + \dfrac{1}{k_{\mathrm{load}}} + \dfrac{1}{k_{\mathrm{d}}}\right)^{-1} \\ k_{\mathrm{eq3}} = \left(\dfrac{1}{k_{\mathrm{m2}}} + \dfrac{1}{k_{\mathrm{t2}}} + \dfrac{1}{k_{\mathrm{m4}}} + \dfrac{1}{k_{\mathrm{r2}}} + \dfrac{1}{k_{\mathrm{m1}}} + \dfrac{1}{k_{\mathrm{t1}}} + \dfrac{1}{k_{\mathrm{m3}}} + \dfrac{1}{k_{\mathrm{r1}}} + \dfrac{1}{k_{\mathrm{load}}} + \dfrac{1}{k_{\mathrm{d}}}\right)^{-1} \end{cases} \tag{12}$$

Where m_{m1}, m_{m2}, m_{m3}, m_{m4}, m_{t1}, m_{t2} and m_{load} represent the mass of the Magnetizer 1, Magnetizer 2, Magnetizer 3, Magnetizer 4, Sleeve 1, Sleeve 2 and output rod, respectively; c_{m1}, c_{m2}, c_{m3}, c_{m4}, c_{t1}, c_{t2}, m_{load} and c_{d} represent the damping of the Magnetizer 1, Magnetizer 2, Magnetizer 3, Magnetizer 4, Sleeve 1, Sleeve 2, output rod and disc spring assembly, respectively; k_{m1}, k_{m2}, k_{m3}, k_{m4}, k_{t1}, k_{t2}, k_{load} and k_{d} represent the stiffness of the Magnetizer 1, Magnetizer 2, Magnetizer 3, Magnetizer 4, Sleeve 1, Sleeve 2, output rod and disc spring assembly, respectively.

Hence, as illustrated in Fig. 8, the procedure for calculating the self-sensing displacement using the theoretical model is as follows: initially, the magnetic induction intensity of the three magnetostrictive rods is calculated using equations (4) and (5). Subsequently, the magnetization of the three rods is obtained through equation (7). Thereafter, the magnetostrictive strain and magnetostrictive force of the three rods are calculated separately by applying equations (8) and (10). Ultimately, these magnetostrictive force are incorporated into equation (11) to derive the displacement of MDMA.

3.2. Real-time displacement self-sensing surrogate model

3.2.1. Model architecture and operational mechanism

Fig. 9 illustrates the architecture and operational mechanism of the RDSSM, which integrates the DWT algorithm with a two-layer MLP network to calculate the predictive displacement by the sampled data from four distinct sets of induction coils over five consecutive time intervals. The figure depicts both the off-line phases of model training and validation, as well as the principle underlying on-line testing.

During the off-line training and validation of MLP, it was necessary to preprocess the four distinct sets of induced current data. Using induced current 1 as an illustrative example, a sliding window of length five was employed to extract induced current sequence $S_1 = [i_{s1}(k), i_{s1}(k{+}1), i_{s1}(k{+}2), i_{s1}(k{+}3), i_{s1}(k{+}4)]$, which consisted of five consecutive time intervals, starting at the sampling instance k. With each incremental shifted of the sliding window by one sample, a new data sequence was obtained. Subsequently, the DWT algorithm was applied to extract three approximation coefficients, labeled as $c_{\mathrm{a1k}}(1)$, $c_{\mathrm{a1k}}(2)$, and $c_{\mathrm{a1k}}(3)$, and two detail coefficients, labeled as $c_{\mathrm{d1k}}(1)$ and $c_{\mathrm{d1k}}(2)$, from induced current sequence S_1. These coefficients, combined with the original induced current sequence, were concatenated to form an sequence of length 10, labeled as $S_2 = [i_{s1}(k), i_{s1}(k{+}1), i_{s1}(k{+}2), i_{s1}(k{+}3), i_{s1}(k{+}4), c_{\mathrm{a1k}}(1), c_{\mathrm{a1k}}(2), c_{\mathrm{a1k}}(3), c_{\mathrm{d1k}}(1), c_{\mathrm{d1k}}(2)]$. Following the same processing of induced current 2, 3, and 4, all the four distinct input sequences were concatenated to form a final sequence of length 40, labeled as $S_3 = [i_{s1}(k), \ldots, i_{s1}(k{+}4), c_{\mathrm{a1k}}(1), \ldots, c_{\mathrm{d1k}}(2), i_{s2}(k), \ldots, i_{s2}(k{+}4), c_{\mathrm{a2k}}(1), \ldots, c_{\mathrm{d2k}}(2), i_{s3}(k), \ldots, i_{s3}(k{+}4), c_{\mathrm{a3k}}(1), \ldots, c_{\mathrm{d3k}}(2), i_{s4}(k), \ldots, i_{s4}(k{+}4), c_{\mathrm{a4k}}(1), \ldots, c_{\mathrm{d4k}}(2)]$. The final sequence S_3 and the displacement $d(k{+}4)$ at the sampling instance $(k{+}4)$ were used as the input and output for the training and validation datasets, respectively. By applying this data preprocessing technique, the input was transformed from four time series data into discrete multidimensional data that incorporates information from five consecutive time intervals. This method could effectively diminish temporal dependency and reduce the risk of temporal leakage that may occur during the random splitting of training and validation datasets.

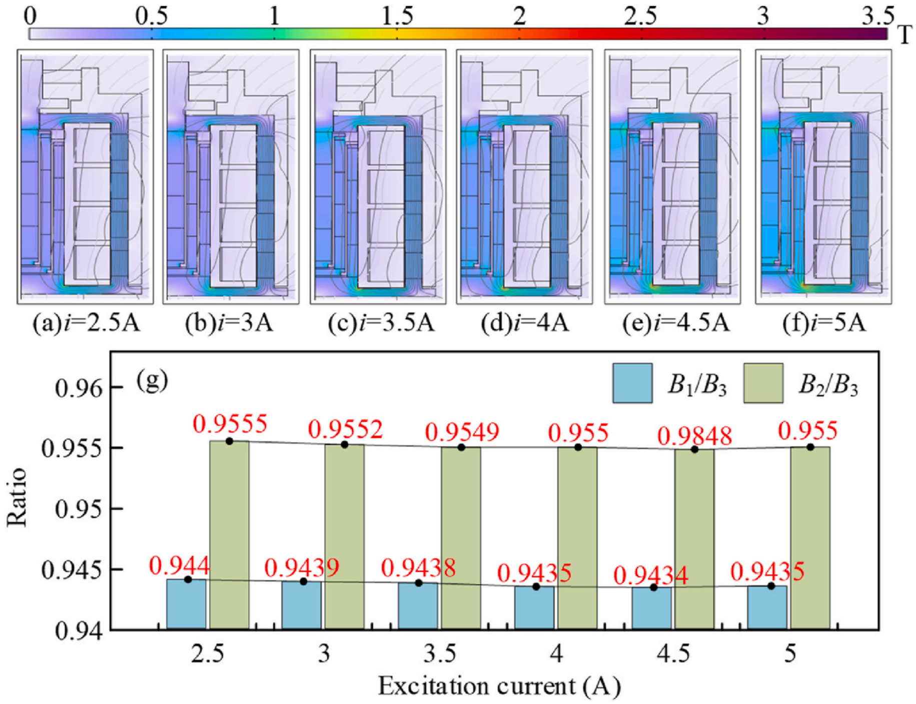

Fig. 6. The magnetic induction intensity simulation results of MDMA.

In the real-time prediction of RDSSM based on the pre-trained MLP network, the processes of induced current acquisition, data extraction, DWT application, and MLP network computation were all performed online and in real-time. The computational methodology was consistent with that used during the model training phase. Notably, the output of MLP network at sampling instance (k+4), labeled as d_p*(k+4), was averaged with d_p*(k+2) and d_p*(k+3) from the two preceding sampling instances (k+2) and (k+3). Finally, the averaged value was smoothed through a low-pass filter with a cutoff frequency of 3000 Hz to produce the model's predicted displacement, labeled as d_p(k+4), at the sampling instance (k+4).

3.2.2. *Working principle of DWT algorithm*

The DWT algorithm offers superior time-frequency localization capabilities, enabling effective analysis of instantaneous characteristics in non-stationary signals. Additionally, it provides advantages such as high computational efficiency and straightforward implementation. In this study, the DWT algorithm was used to decompose the induced current sequence, labeled as [i_s(k), i_s(k+1), i_s(k+2), i_s(k+3), i_s(k+4)], into sub-bands corresponding to various frequency components and temporal scales. From these sub-bands, approximate and detail coefficients were extracted as feature data. This approach enriched the feature representation of the input signals, thereby significantly improving the predictive accuracy of the RDSSM within specified frequency and amplitude

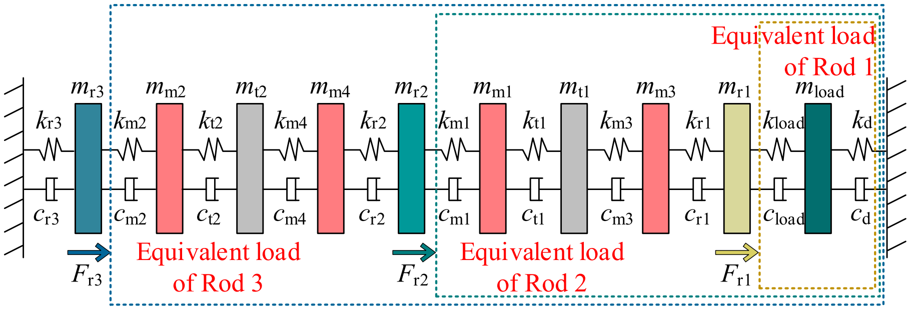

Fig. 7. The schematic of the multibody mechanical dynamic system of the MDMA.

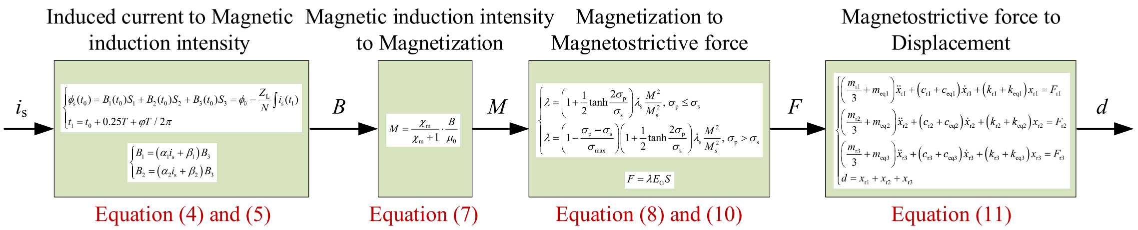

Fig. 8. The procedure for calculating the self-sensing displacement using the theoretical model.

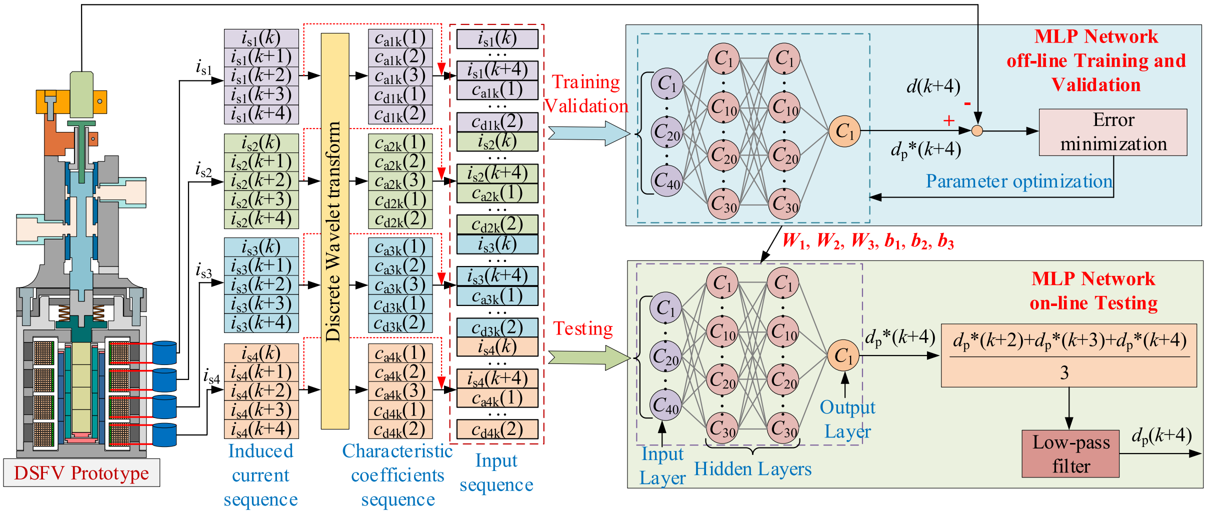

Fig. 9. The architecture and operational mechanism of the RDSSM.

domains.

In this study, the "Haar" wavelet function was chosen to process the induced current signal, with the coefficients of the low-pass filter F_{low} and high-pass filter F_{high} shown as follows:

$$\begin{cases} F_{\text{low}} = \left[1\big/\sqrt{2} \quad 1\big/\sqrt{2}\right] \\ F_{\text{high}} = \left[1\big/\sqrt{2} \quad -1\big/\sqrt{2}\right] \end{cases} \tag{13}$$

For the induced current sequence [$i_s(k)$, $i_s(k+1)$, $i_s(k+2)$, $i_s(k+3)$, $i_s(k+4)$], the approximate coefficients and the detail coefficients are calculated through the following equations:

$$\begin{cases} c_a(1) = \frac{1}{\sqrt{2}} i_s(k) + \frac{1}{\sqrt{2}} i_s(k+1) \\ c_a(2) = \frac{1}{\sqrt{2}} i_s(k+2) + \frac{1}{\sqrt{2}} i_s(k+3) \\ c_a(3) = \frac{1}{\sqrt{2}} i_s(k+4) \\ c_d(1) = \frac{1}{\sqrt{2}} i_s(k) - \frac{1}{\sqrt{2}} i_s(k+1) \\ c_d(2) = \frac{1}{\sqrt{2}} i_s(k+2) - \frac{1}{\sqrt{2}} i_s(k+3) \end{cases} \tag{14}$$

3.2.3. *Working principle of MLP network*

As illustrated in Fig. 9, the MLP network consisted of three distinct layers: the input layer, the hidden layer, and the output layer. The input layer, with a dimensionality of 40, was designed to accept an input vector comprising four sets of induced currents along with feature values extracted using the DWT algorithm. The hidden layer was composed of two neuron layers, each containing 30 neurons, which performed feature extraction and transformation of the input data. Finally, the output layer produced the predicted displacement. The computational process of the MLP network is as follows:

Step 1: The input vector $\boldsymbol{x}$ is transformed linearly by the weight matrix $\boldsymbol{W_1}$ and bias vector $\boldsymbol{b_1}$, followed by the application of a nonlinear activation function h, producing the output $\boldsymbol{a_1}$ of the first hidden layer, as expressed:

$$\boldsymbol{a}_1 = h(\boldsymbol{W}_1\boldsymbol{x} + \boldsymbol{b}_1) = \max(0, \boldsymbol{W}_1\boldsymbol{x} + \boldsymbol{b}_1) \tag{15}$$

Step 2: The output vector $\boldsymbol{a_1}$ of the first hidden layer is transformed linearly by the weight matrix $\boldsymbol{W_2}$ and bias vector $\boldsymbol{b_2}$, followed by the application of a nonlinear activation function h, producing the output $\boldsymbol{a_2}$ of the second hidden layer, as expressed:

$$\boldsymbol{a}_2 = h(\boldsymbol{W}_2\boldsymbol{a}_1 + \boldsymbol{b}_2) = \max(0, \boldsymbol{W}_2\boldsymbol{a}_1 + \boldsymbol{b}_2) \tag{16}$$

Step 3: The output vector $\boldsymbol{a_2}$ of the second hidden layer is transformed linearly by the weight matrix $\boldsymbol{W_3}$ and bias vector $\boldsymbol{b_3}$, followed by the application of a linear activation function g, producing the output $\boldsymbol{y}$ of the output layer, as expressed:

$$\boldsymbol{y} = g(\boldsymbol{W}_3\boldsymbol{a}_2 + \boldsymbol{b}_3) = \boldsymbol{W}_3\boldsymbol{a}_2 + \boldsymbol{b}_3 \tag{17}$$

Where $\boldsymbol{x}$ = [$i_{s1}(k)$, …, $i_{s1}(k+4)$, $c_{a1k}(1)$, …, $c_{d1k}(2)$, $i_{s2}(k)$, …, $i_{s2}(k+4)$, $c_{a2k}(1)$, …, $c_{d2k}(2)$, $i_{s3}(k)$, …, $i_{s3}(k+4)$, $c_{a3k}(1)$, …, $c_{d3k}(2)$, $i_{s4}(k)$, …, $i_{s4}(k+4)$, $c_{a4k}(1)$, …, $c_{d4k}(2)$] $\in \boldsymbol{R}^{40}$; $\boldsymbol{a_1}$, $\boldsymbol{a_2}$, $\boldsymbol{b_1}$, $\boldsymbol{b_2} \in \boldsymbol{R}^{30}$; $\boldsymbol{W_1} \in \boldsymbol{R}^{30\times40}$; $\boldsymbol{W_2} \in \boldsymbol{R}^{30\times30}$; $\boldsymbol{W_3} \in \boldsymbol{R}^{10\times30}$; $\boldsymbol{b_3}$, $\boldsymbol{y} \in \boldsymbol{R}^{1}$. Among them, the values of $\boldsymbol{W_1}$, $\boldsymbol{W_2}$, $\boldsymbol{W_3}$, $\boldsymbol{b_1}$, $\boldsymbol{b_2}$ and $\boldsymbol{b_3}$ were obtained through the training and optimization of the RDSSM model.

4. Experimental evaluation

In this section, a prototype of the DSFV was fabricated, and a series of experiments were conducted to validate the accuracy of the proposed theoretical model, as well as the RDSSM. To ensure the generalization capability of the MLP network, the amplitude of the excitation current was limited to the range of 2.8 A to 4.8 A, and the frequency was restricted to between 400 Hz and 700 Hz. Furthermore, all experiments were conducted at an ambient temperature around 20 °C.

4.1. *Prototype fabrication and experimental platform*

Fig. 10 illustrates the constituent elements of the DSFV prototype. Among these, the three magnetostrictive rods were fabricated from Terfenol-D material. To ensure the functionality of MDMA at elevated temperatures, the permanent magnets were made of samarium-cobalt, which has a Curie temperature of up to 700 °C. Meanwhile, the coil frame was constructed from Polyether-Ether-Ketone (PEEK), a polymer capable of maintaining normal operation at temperatures up to 250 °C. The excitation and induction coils were fabricated using copper enameled wire with outer diameters of 0.6 mm and 0.3 mm, respectively. Each induction coil, with a parasitic capacitance of 0.23 nF, consisted of a single layer with 29 turns, resulting in a winding density of 2.78 turns per millimeter. In contrast, each excitation coil comprised 13 layers with a total of 168 turns, exhibiting an axial winding density of 1.24 turns per millimeter and a radial winding density of 1.63 turns per millimeter. The magnetizers and valve body were manufactured from DT4C material, whereas the inner and outer spools were made from SUS304 stainless steel. The axial and radial dimensions of the principal components within the DSFV prototype are detailed in Table 4.

Based on the DSFV prototype, the schematic diagram and the physical configuration of the experimental platform are illustrated in Figs. 11 and 12, respectively. The experimental platform primarily consisted of a real-time simulator (Speedgoat GmbH, Performance P3), four power amplifiers (AETechron Inc., 7224), a capacitive displacement sensor (Harbin Core Tomorrow Technology Co., Ltd., E09.Cap), four current sensors (Nanjing Zhenhengtong Electronics Co., Ltd., ZHTBCT 1A/5.3V), and a DSFV prototype. Prior to factory dispatch, the capacitive sensor and the current sensors underwent individual calibration procedures using a laser interferometer and a current transformer tester, respectively. This process ensured the accurate measurement of displacement and induced current during experimentation, thereby validating the precision of the self-sensing displacement model. Furthermore, the sensors' data were simultaneously sampled by the IO324-200K board integrated within the real-time simulator, which achieves nanosecond-level time alignment accuracy for multi-channel signal acquisition, thereby effectively ensuring precise time alignment between the displacement sensor and current sensors. The performance parameters of the capacitive displacement sensor and current sensors are presented in Table 5.

Notably, the VCM was removed from the DSFV prototype to enable direct measurement for the actual displacement of the inner spool using the capacitive displacement sensor. The real-time simulator interfaced with the host computer, managing signal transmission and reception while executing the simulation model. In this system, each power amplifier was connected in series with a corresponding set of excitation coils of the MDMA, converting the driving voltage signal from the real-time simulator into a proportional excitation current. Meanwhile, the four current sensors were responsible for measuring the induced current signals generated in the four sets of induction coils of the MDMA. To ensure precise sampling of high-frequency signals without distortion, the step size of the Simulink simulation model was set to 2×10^{-5} s, thereby synchronizing both the signal sampling interval and the model computation interval to this value.

4.2. *Parameter identification of the theoretical model*

4.2.1. *Phase lag correction of the induced current*

In the open-loop excitation experiments conducted on the MDMA, measurements of the induced current and displacement were obtained. However, due to the induced current lags behind the magnetic flux by an angle of $(\pi/2 + \varphi)$, it is essential to correct the phase lag of the induced current sequence to match the displacement sequence. The principle of this correction procedure is illustrated in Fig. 13.

Firstly, based on the frequency f_0 of the excitation current, the number of sampling points k by which the induced current lagged behind the displacement was calculated by following equation:

Table 4
The axial and radial dimensions of the principal components within the DSFV prototype.

Component	Rod 1	Rod 2	Rod 3	MDMA	Inner Spool	Outer Spool	DSFV
Inner diameter (mm)	0	9	15	0	0	10	0
Outer diameter (mm)	8	14	20	56	10	14	56
Length (mm)	40	40	40	72	39	28	139

$$k = \left(\frac{0.25}{f_0} + \frac{\arctan\left(\frac{2\pi f_0 L}{R_L}\right)}{2\pi f_0} \right) \times \frac{1}{T_s} \tag{18}$$

Where T_s represents the sampling time step. Subsequently, the induced current sequence $[i_s(k+1), i_s(k+2), \ldots, i_s(k + \text{n-1}), i_s(k + \text{n})]$ was extracted to serve as the input for the off-line calculation of the theoretical model. Finally, the output displacement of the theoretical model was compared with the measured displacement sequence $[d(1), d(2), \ldots, d(\text{n-1}), d(\text{n})]$ to assess the accuracy of the theoretical model.

4.2.2. *Parameter identification results*

In the theoretical model of the self-sensing displacement, certain parameters such as size, mass, and stiffness can be directly measured or calculated, as shown in Table 6.

In contrast, parameters such as damping, preload, and the initial magnetic flux of the induction coil must be determined through parameter identification methods based on experimental data. In this study, a multi-island genetic algorithm was employed to estimate these parameters in the "Isight" software. As illustrated in Fig. 14, the experimental data acquired under three distinct sinusoidal excitation conditions were preprocessed and subsequently employed for parameter identification, with four periods selected for each dataset.

The principle and process of parameter identification are illustrated in Fig. 15, in which d_{sim1}, d_{sim2} and d_{sim3} represent the displacements of the theoretical model under excitation conditions (a), (b) and (c), respectively. Correspondingly, d_{exp1}, d_{exp2} and d_{exp3} represent the experimental displacements of the MDMA under the same respective conditions. Throughout the parameter identification process, both the maximum errors, labeled as $e_{1\text{max}}$, $e_{2\text{max}}$, and $e_{3\text{max}}$, and the root mean square errors, labeled as, $e_{1\text{rms}}$, $e_{2\text{rms}}$, and $e_{3\text{rms}}$, between the model results and the experimental data were calculated and used as the objective function:

$$f(x) = e_{1\text{ max}} + e_{2\text{ max}} + e_{3\text{ max}} + e_{1\text{rms}} + e_{2\text{rms}} + e_{3\text{rms}} + e_{\text{a}} \tag{19}$$

Where e_{a} was employed to restrict the extent of dispersion of parameter identification results under three different excitation conditions, and it was calculated by the following equation:

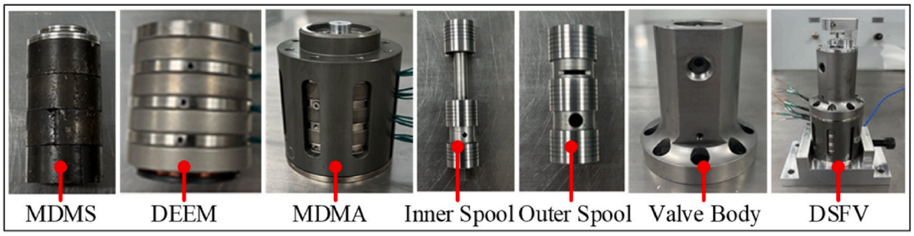

Fig. 10. The constituent elements of the DSFV prototype.

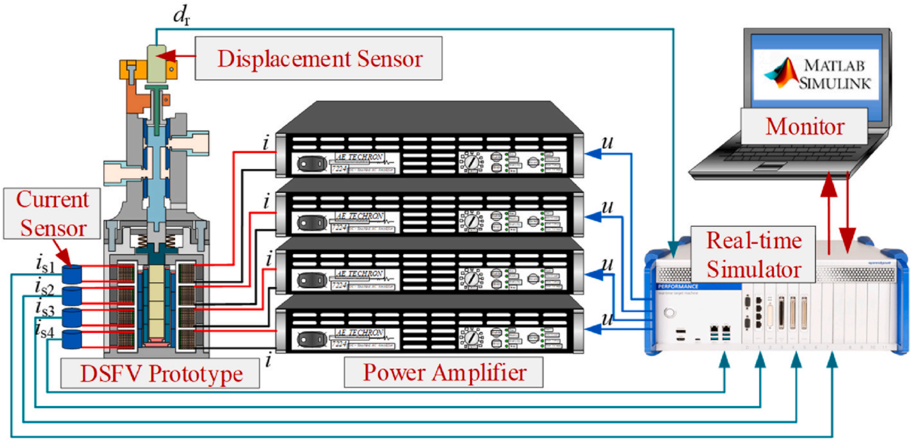

Fig. 11. The schematic diagram of the experimental platform.

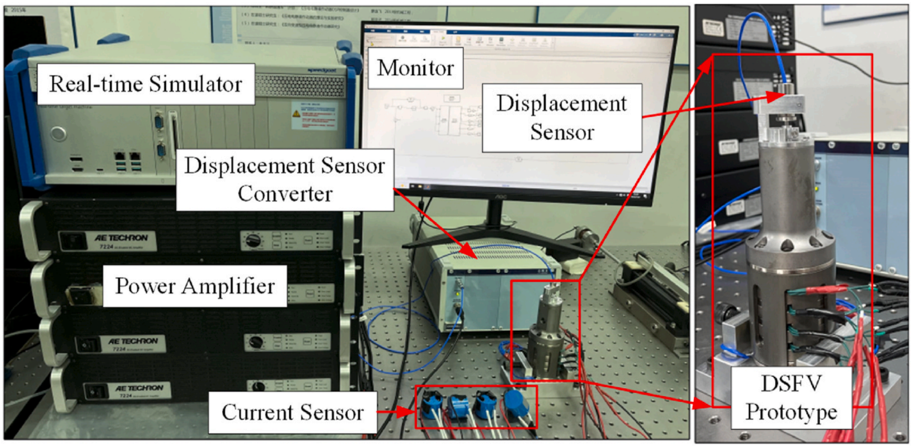

Fig. 12. The physical configuration of the experimental platform.

Table 5
The performance parameters of the capacitive displacement sensor and current sensors.

Sensor	Range	Resolution	Linearity	Signal-to-noise ratio	Temperature drift
Capacitive displacement sensor	0–200 μm	0.02 %F.S.	0.05 %F.S.	54 dB	0.005 %FSO/°C
Current sensor	±1A	0.05 %F.S.	0.05 %F.S.	60 dB	0.01 %FSO/°C

$$\begin{cases} e_a = \sqrt{\frac{1}{3}\left[(e_{1\text{rms}} - e_m)^2 + (e_{2\text{rms}} - e_m)^2 + (e_{3\text{rms}} - e_m)^2\right]} \\ e_m = \frac{1}{3}(e_{1\text{rms}} + e_{2\text{rms}} + e_{3\text{rms}}) \end{cases} \tag{20}$$

Consequently, the parameter identification of theoretical model was transformed into a multi-variable multi-objective optimization process, that was, determining a set of parameters to minimize the objective function. The parameters setting of the multi-island genetic algorithm and the results of the identification parameter are presented in Tables 7 and 8, respectively.

4.3. Training and validation of the RDSSM

Using the experimental platform shown in Fig. 12, a series of 22 sinusoidal frequency sweep excitation tests with varying amplitudes were conducted on the DSFV prototype to generate the training and validation datasets for the RDSSM. The amplitude of the sinusoidal sweep current ranged from 2.8 A to 4.8 A, increasing in increments of 0.1 A between each successive experiment. Specifically, the sweep signal frequency increased linearly from 400 Hz to 700 Hz over 0.4 s in each trial. After applying the DWT algorithm and normalizing the acquired data, a total of 659824 data samples were obtained. These samples were then randomly divided into training and validation subsets in an 80:20 ratio. The configuration parameters utilized for training the RDSSM are presented in Table 9. Notably, the training process was terminated if the loss did not exhibit a reduction over 20 consecutive iterations.

The predictive performance on both the training and validation datasets is shown in Figs. 16 and 17, respectively. Within the training datasets, 83.52 % of the prediction errors were within 1 μm, and 98.03 % were within 2 μm. Similarly, in the validation datasets, 82.43 % of the errors fell within 1 μm, and 97.76 % were within 2 μm. These results demonstrated that the RDSSM achieved both a high level of fitting accuracy and strong generalization capability, but further validation using additional testing datasets remained necessary.

4.4. Modeling results analysis

In Section 4.2, the parameters of the theoretical model were identified through multi-island genetic algorithm, based on the experimental data of three distinct excitation current conditions. And in Section 4.3, the RDSSM was trained well based on the experimental data of 22

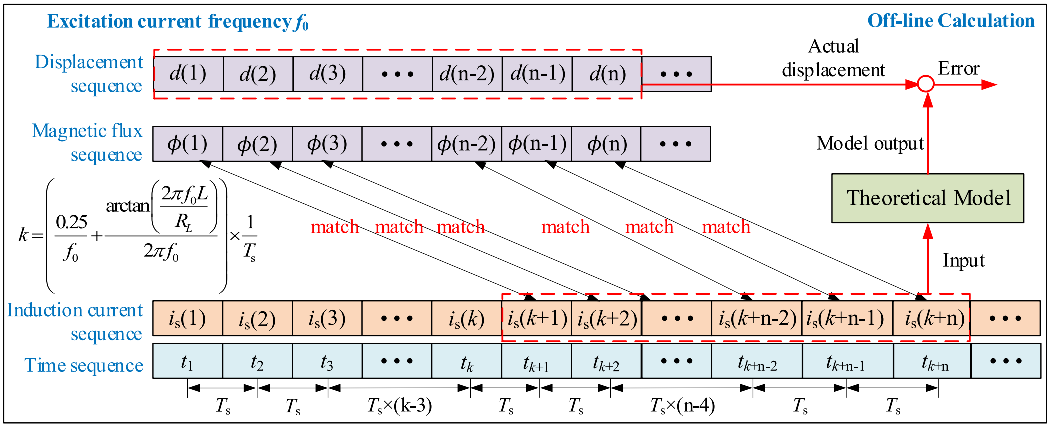

Fig. 13. The principle of phase lag correction procedure of the induced current.

Table 6
The measured parameter values of the theoretical model.

Symbol	Unit	Value	Symbol	Unit	Value	Symbol	Unit	Value
m_{r1}	g	18.6	m_{load}	g	27.1	k_{t2}	N/μm	117.29
m_{r2}	g	33.4	k_{r1}	N/μm	37.7	k_{load}	N/μm	642
m_{r3}	g	50.9	k_{r2}	N/μm	67.74	k_d	N/μm	0.21
m_{m1}	g	0.72	k_{r3}	N/μm	103.08	E_G	GPa	30
m_{m2}	g	1.09	k_{m1}	N/μm	2077.38	M_s	A/m	6×10^5
m_{m3}	g	0.72	k_{m2}	N/μm	3161.23	λ_s	–	0.001
m_{m4}	g	2.12	k_{m3}	N/μm	506	μ_0	H/μm	1.26
m_{t1}	g	5.29	k_{m4}	N/μm	505.79	R_L	Ω	10
m_{t2}	g	8.93	k_{t1}	N/μm	68.75	L	mH	0.89

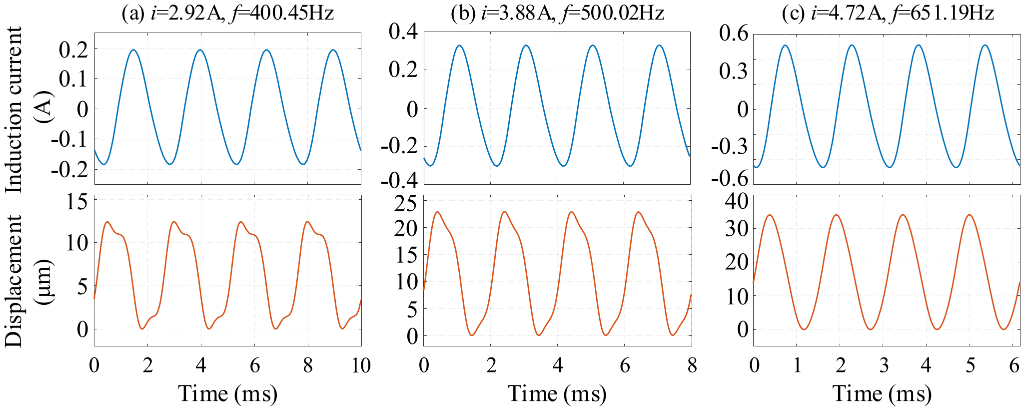

Fig. 14. The datasets used for parameter identification of theoretical model.

sinusoidal frequency sweep excitation tests. In this section, eight groups of distinct sets of sinusoidal excitation current conditions, each characterized by varying amplitudes and frequencies, were applied to comparatively test and evaluate the modeling accuracy of both the theoretical model and the RDSSM. It is important to further note that, among the eight groups of distinct sets of sinusoidal excitation current conditions, three groups were consistent with those used for parameter identification in Section 4.2. However, all the eight groups differed from the 22 sinusoidal frequency sweep excitation tests in Section 4.3. In addition, this study also performed a comparative analysis for several models based on the RDSSM and theoretical model. Specifically:

(a) Model 1: The DWT and MLP-based RDSSM, which was established in Section 3.2.1;
(b) Model 2: The MLP-based RDSSM, which did not include the DWT algorithm;
(c) Model 3: The DWT and Gauss Process Regression (GPR)-based RDSSM, which replaced the MLP network of Model 1 with GPR algorithm.
(d) Model 4: The theoretical model, which was established in Section 3.1;
(e) Model 5: The theoretical model, which described the distribution ratios of B_1, B_2 and B_3 by a nonlinear second-order polynomial function of the induced current, is expressed as:

$$\begin{cases} B_1 = \left(4.02i_s^2 + 0.15i_s + 0.97\right)B_3 \\ B_2 = \left(3.71i_s^2 + 0.18i_s + 0.93\right)B_3 \end{cases} \tag{21}$$

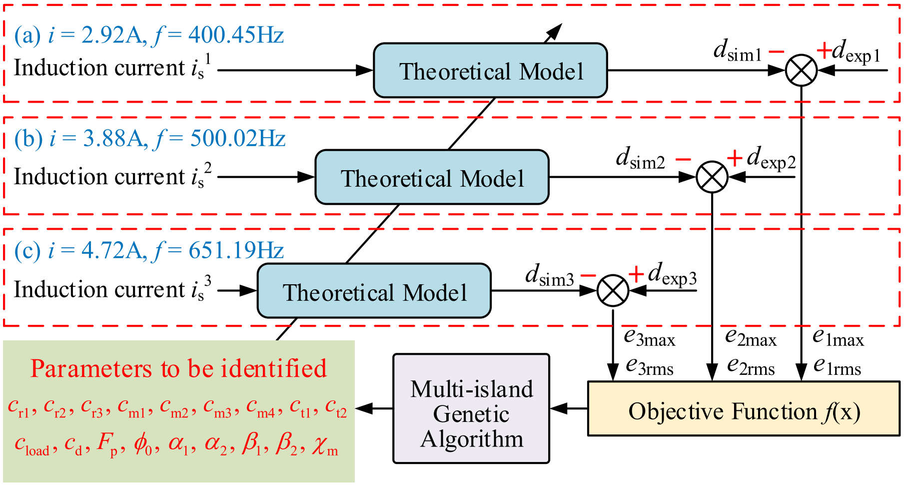

Fig. 15. The process of parameter identification based on multi-island genetic algorithm.

Table 7
The parameters setting of the multi-island genetic algorithm.

Parameter	Value	Parameter	Value
Sub-population size	20	Rate of mutation	0.01
Number of islands	20	Rate of migration	0.01
Number of generations	20	Interval of migration	5
Rate of crossover	1.0	Elite size	1

(f) Model 6: The theoretical model, which did not use the phase lag correction method to process the induced current data.

It should be noted that the results of the Model 3, 4, 5 and 6 were obtained through off-line computations based on the experimental data, while those of the Model 1 and 2 were generated via real-time calculations on the real-time simulator.

Due to variations in geometry, dimensions, magnetic field distribution, and magnetization process, the magnetic susceptibility χ_m of the three magnetostrictive rods differed in different experimental sets. Consequently, for each experimental set, χ_m of the three magnetostrictive rods were identified based on the experimental data specific to that set, in accordance with the procedure illustrated in Fig. 15. Table 10 presents the amplitude and frequency of the excitation current applied across the eight previously described experimental groups. Additionally, the corresponding values of χ_m for each rod, determined through system identification methods, are also presented in the same table.

Fig. 18 presents the results of the open-loop experiments alongside the predictions of the six self-sensing displacement models and their corresponding absolute errors. Specifically, subfigures (a) to (h) represent Groups One to Eight, respectively. Analysis of these results indicates that the displacement trajectories predicted by the model 1, 2, 3, 4, and 5 generally aligned well with the experimental measurements. However, a notable divergence existed between the predicted curves of Model 6 and the experimental measurements, with the phase of the predicted curves lagging behind that of the experiments. This observation suggests that, when reconstructing displacement through the theoretical model, it is essential to apply a correction for the phase lag of the induced current. Furthermore, a systematic deviation was observed between the theoretical model predictions and the empirical data. Within the frequency range of 400 Hz to 600 Hz, particularly during transitions of the displacement from peak to decline or from trough to rise, the measured displacement curves exhibited distinct concave and convex inflection points. These subtle variations, attributable to the intrinsic output characteristics of the MDMA, were not adequately captured by the theoretical model, resulting in significant errors at these critical junctures. In contrast, the RDSSM, trained and optimized using the open-loop experimental data, effectively captured these inherent output features. Consequently, the displacement predictions generated by the RDSSM showed closer agreement with the measured data than those derived from the theoretical model.

Fig. 19 presents the error analysis for model 1, 2, 3, 4, and 5, each compared against the measured data across the experimental groups. Specifically, subfigures (a) to (c) illustrate the maximum error, the average error, and the root mean square error, respectively. The results indicate that all the five models generally maintained relatively low error magnitudes. Notably, the three RDSSM models achieved relatively lower error values, while the two theoretical models exhibited higher error levels.

Table 9
The configuration parameters for training the RDSSM.

Parameter	Setting
Optimizer	Adam
Learning rate	0.01
Batch size	128
Number of epochs	1000
Initialization method	He
Activation function	ReLU
Loss function	Mean square error

Table 8
The identification parameter values of the theoretical model.

Symbol	Unit	Value	Symbol	Unit	Value	Symbol	Unit	Value
c_{r1}	$\text{N}\cdot\text{s}\cdot\text{m}^{-1}$	296.58	c_{m4}	$\text{N}\cdot\text{s}\cdot\text{m}^{-1}$	3613.31	ϕ_0	$\text{T}\cdot\text{m}^2$	0.002
c_{r2}	$\text{N}\cdot\text{s}\cdot\text{m}^{-1}$	4254.32	c_{t1}	$\text{N}\cdot\text{s}\cdot\text{m}^{-1}$	1489.61	α_1	–	0.18
c_{r3}	$\text{N}\cdot\text{s}\cdot\text{m}^{-1}$	630.3	c_{t2}	$\text{N}\cdot\text{s}\cdot\text{m}^{-1}$	2732.6	α_2	–	0.15
c_{m1}	$\text{N}\cdot\text{s}\cdot\text{m}^{-1}$	1302.54	c_{load}	$\text{N}\cdot\text{s}\cdot\text{m}^{-1}$	2192.98	β_1	–	0.96
c_{m2}	$\text{N}\cdot\text{s}\cdot\text{m}^{-1}$	4631.56	c_d	$\text{N}\cdot\text{s}\cdot\text{m}^{-1}$	2286.27	β_2	–	0.94
c_{m3}	$\text{N}\cdot\text{s}\cdot\text{m}^{-1}$	3613.31	F_p	N	510.47			

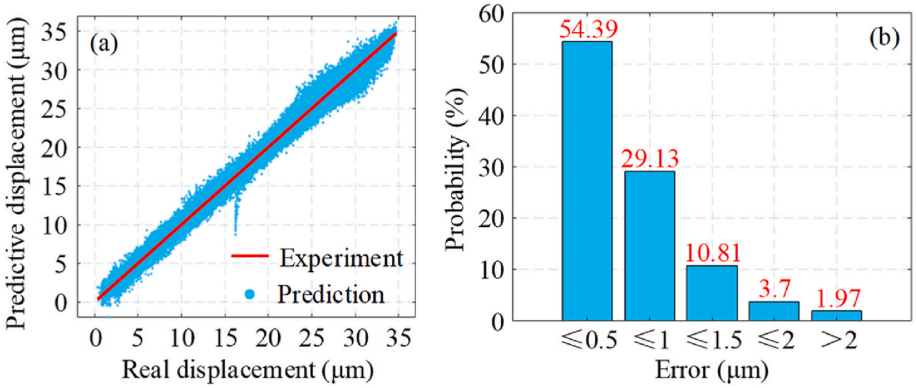

Fig. 16. The predictive performance on the training datasets.

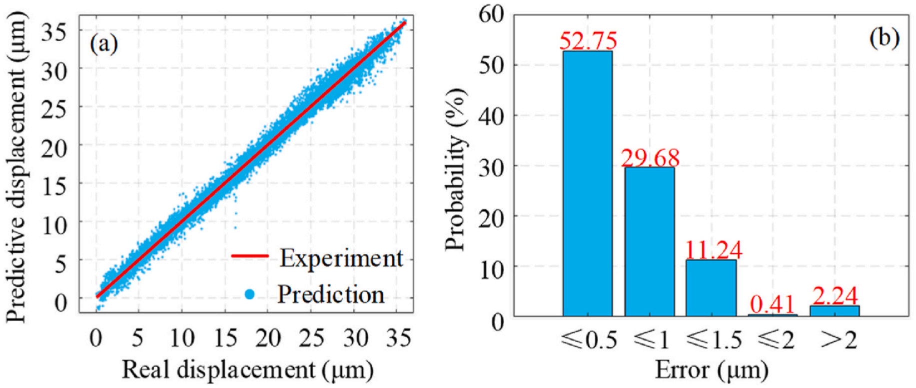

Fig. 17. The predictive performance on the validation datasets.

Table 10
The amplitude and frequency of the excitation current and the values of χ_{m} for each rod.

Group	One	Two	Three	Four	Five	Six	Seven	Eight
Amplitude (A)	2.92	4.6	3.28	3.88	3	3.68	4.72	3.12
Frequency (Hz)	400.45	451.67	450.92	500.02	501.11	599.78	651.19	680.76
χ_{m} of Rod 1	2.47	6.66	5.71	3.93	3.04	6.94	7.47	10.97
χ_{m} of Rod 2	1.21	3.99	3.14	3.02	2.12	6.02	6.41	9.41
χ_{m} of Rod 3	3.28	2.45	1.59	6.08	5.18	9.08	7.28	10.27

Due to variations in excitation currents across the experimental sets, the maximum displacement of the MDMA exhibited significant differences, rendering subtraction error an inadequate metric for assessing the modeling error of the self-sensing displacement models. Therefore, this study quantified the modeling error of each model by calculating the ratio of the average error to the maximum displacement, as shown below:

$$\mathrm{Error} = \frac{e_{\mathrm{Average}}}{d_{\mathrm{Maximum}}} \times 100\% \tag{22}$$

Where e_{Average} represents the average error, and d_{Maximum} represents the maximum displacement of the MDMA.

The modeling error results presented in Table 11 showed that the average errors across the eight experimental groups of Model 1, 2, 3, 4, and 5 stayed under 6 %, while that of Model 6 exceeded 69 %. Notably, the Model 1 exhibited the lowest error rate at 3.63 %, which was 0.61 % lower than the 4.24 % error observed for Model 2 and 1.72 % lower than the 5.35 % error for Model 3. Additionally, the average error of Model 4 and Model 5 were 5.34 % and 5.48 %, respectively, which indicated that both the linear first-order polynomial function and the nonlinear second-order polynomial function achieved high accuracies to describe the magnetic induction intensity distribution rates of the three magnetostrictive rods. However, the linear model was simpler compared to the nonlinear model.

4.5. *Comparison of real-time performance of the models*

To facilitate a more comprehensive comparison of the computational efficiency between Model 1, Model 3, and Model 4, the average computation time per sampling step of Model 3 and Model 4 in the computer were measured and analyzed, alongside that of Model 1 implemented in the real-time simulator, with the corresponding results presented in Fig. 20. Furthermore, the real-time margin of Model 1 is illustrated in Fig. 20, and the corresponding calculation equation is as follows:

$$\mathrm{Margin} = 1 - \frac{T_{\mathrm{R}}}{T_{\mathrm{s}}} \times 100\% \tag{23}$$

Where T_{R} represent the average computation time per sampling step of Model 1 in real-time simulator; T_{s} represent the time step of the real-time simulator, with a value of 20 μs.

The results indicated that Model 3 and Model 4 required an average

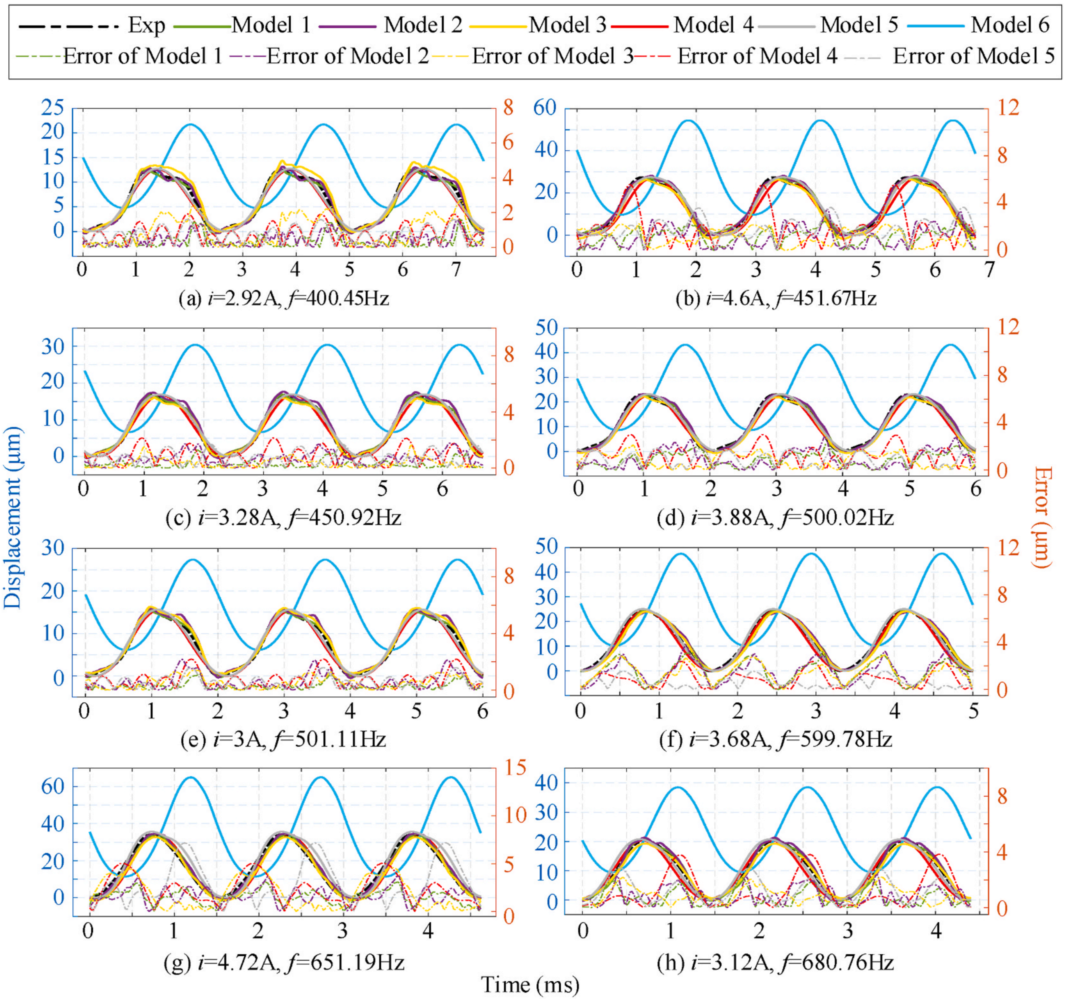

(a) i=2.92A, f=400.45Hz (b) i=4.6A, f=451.67Hz

(c) i=3.28A, f=450.92Hz (d) i=3.88A, f=500.02Hz

(e) i=3A, f=501.11Hz (f) i=3.68A, f=599.78Hz

(g) i=4.72A, f=651.19Hz (h) i=3.12A, f=680.76Hz

Fig. 18. The results and absolute errors of the several comparative models.

computation time per sampling step of 26.94 ms and 48.69 μs in computer, which significantly exceeded the 20 μs time step of the real-time simulator. Notably, the hardware configuration of the computer (CPU: Intel Core i7-14700KF 3.40 GHz; Running memory: 64 GB; Disk storage: 2 TB SSD; GPU: NVIDIA GeForce RTX 4060 8 GB) surpassed that of the real-time simulator (CPU: Intel Core 3.10 GHz; Running memory: 8 GB; Disk storage: 128 GB SSD; GPU: None), suggesting that the computational efficiencies of Model 3 and Model 4 were insufficient to satisfy the requirement at a sampling and calculation frequency of 50 kHz in the real-time simulator. Conversely, Model 1 demonstrated an average computation time per sampling step of 11.58 μs in real-time simulator and preserved an average real-time margin of 42.09 %, which afforded a relatively ample temporal allowance for the implementation of simple linear control algorithms. The finding suggested that the RDSSM was feasible to be ported to embedded controllers with comparatively limited computational resources. Furthermore, typical embedded controllers, such as FPGA and DSP, offer robust parallel processing and signal processing functionalities, thereby providing a suitable platform for optimizing model architectures and facilitating high-frequency data acquisition.

5. Closed-loop control test based on the RDSSM

As detailed in Section 4.4, the RDSSM effectively predicted the displacement of the inner spool across a range of open-loop tests with varying excitation currents. However, the primary objective of the RDSSM is to replace the displacement sensor within the closed-loop control system of the inner spool, thereby enabling accurate self-sensing, feedback, and control of its displacement. Accordingly, this section presented series closed-loop control experiments conducted on the inner spool, using both the model-predicted displacement and the directly measured displacement as feedback signals, to further validate the modeling accuracy and performance of the RDSSM.

5.1. *Principle and components of closed-loop control system*

Due to the significant hysteresis characteristic of the magnetostrictive actuators, where the displacement lags behind the excitation current, this study employed a hybrid control strategy integrating both feedforward and feedback mechanisms. The feedforward controller was developed based on the inverse model of the MDMA, enabling the computation of a compensation signal to mitigate hysteresis-induced errors originating from the input signal. Simultaneously, a proportional-integral (PI) feedback controller was implemented to dynamically regulate the output, thereby enhancing overall control accuracy.

The architecture and principle of the closed-loop control system for the inner spool are illustrated in Fig. 21. Specifically, the feedback variable in subfigure (a) was the predictive displacement of the RDSSM, whereas that in subfigure (b) was the displacement measured by the displacement sensor.

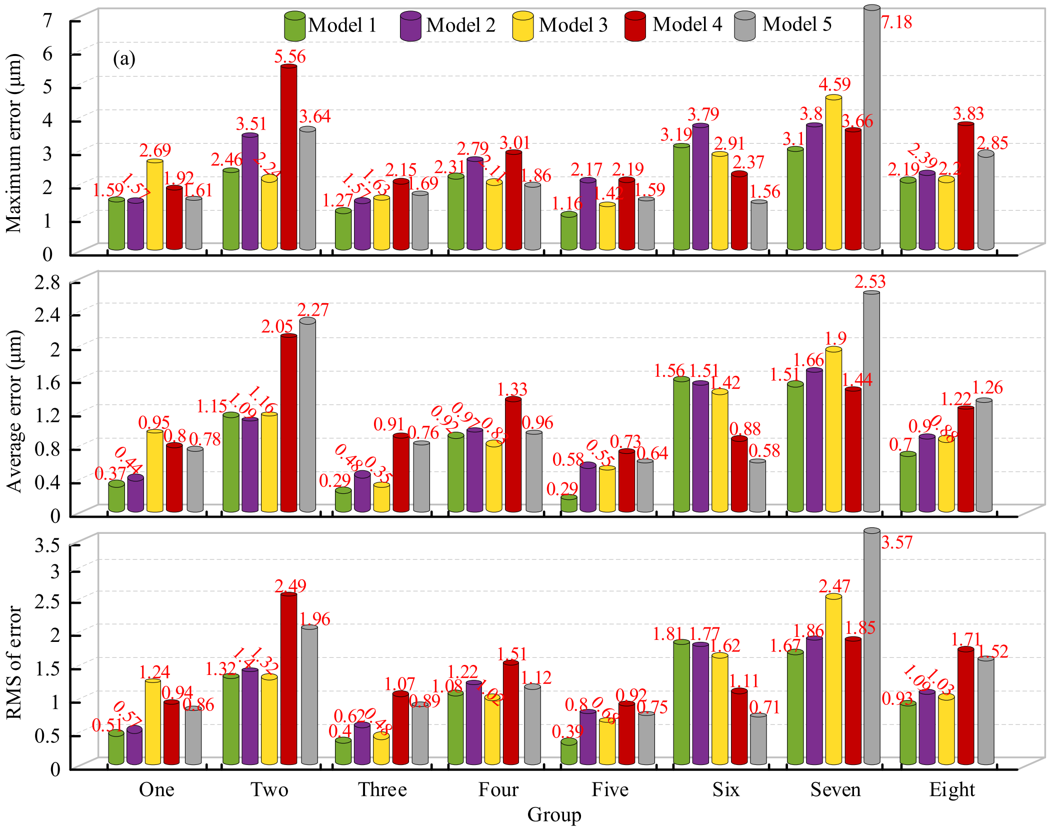

Fig. 19. The specific values of the errors of the several self-sensing displacement models.

Table 11
The comparison of modelling errors of the several self-sensing displacement models.

Group	One	Two	Three	Four	Five	Six	Seven	Eight	Average
Model 1	2.95 %	4.22 %	1.72 %	4.03 %	1.9 %	6.36 %	4.42 %	3.48 %	3.63 %
Model 2	3.53 %	4 %	2.86 %	4.25 %	3.75 %	6.16 %	4.88 %	4.47 %	4.24 %
Model 3	7.63 %	4.26 %	2.07 %	3.63 %	3.56 %	6.18 %	5.58 %	4.36 %	5.35 %
Model 4	6.43 %	7.54 %	5.46 %	5.83 %	4.74 %	3.58 %	4.22 %	6 %	5.48 %
Model 5	6.29 %	8.34 %	4.53 %	4.18 %	4.17 %	2.35 %	7.4 %	6.2 %	5.43 %
Model 6	62.43 %	76.04 %	68.7 %	70.25 %	64.65 %	71.18 %	71.99 %	67.8 %	69.13 %

5.2. *Inverse model of the MDMA*

In this study, a sinusoidal frequency sweep experiment with a current amplitude of 3 A, during which the frequency was linearly varied from 10 Hz to 2000 Hz over 4 s, was conducted to characterize the dynamic response of the MDMA. Using a parameter identification method, a second-order model $G_n(s)$ was derived to represent the nominal model of the MDMA. The corresponding transfer function of $G_n(s)$ is as follows:

$$G_n(s) = \frac{9.178 \times 10^8}{s^2 + 3020s + 81662737} \tag{24}$$

Fig. 22 presents the amplitude-frequency and phase-frequency response curves of the MDMA prototype compared to those of the nominal model. The results demonstrated a close correspondence between the amplitude and phase characteristics of the physical prototype and the nominal model. Notably, the resonance frequencies of the physical prototype and the nominal model were 1411.38 Hz and 1402.63 Hz, respectively, indicating a discrepancy of 8.75 Hz. The gains at resonance were 24.62 dB for the physical prototype and 23.71 dB for the nominal model, with a difference of 0.91 dB. Furthermore, the phase bandwidths were determined to be 1419.38 Hz for the physical prototype and 1584.25 Hz for the nominal model, yielding a difference of 164.84 Hz. These results substantiated the nominal model's validity in accurately representing the behavior of the MDMA prototype.

Applying the inverse operation to $G_n(s)$, the inverse model of the MDMA was obtained, denoted as $G_n^{-1}(s)$. However, the numerator order of $G_n^{-1}(s)$ exceeded that of the denominator, making $G_n^{-1}(s)$ unstable and physically unrealizable. To address this problem, this study introduced a cascade configuration of $G_n^{-1}(s)$ combined with a low-pass filter, denoted as $Q(s) = 1/(2.5 \times 10^{-7}s^2 + 0.001s + 1)$. Consequently, the transfer function of the inverse model of MDMA, denoted as $G_{IM}(s)$, is expressed as follows:

$$G_{IM}(s) = Q(s)G_n^{-1}(s) = \frac{s^2 + 3020s + 81662737}{229.4s^2 + 917800s + 9.18 \times 10^8} \tag{25}$$

5.3. *Closed-loop control results analysis*

According to the closed-loop control system framework shown in Fig. 21(a), this study developed a Simulink real-time simulation model for the closed-loop control of the inner spool, as shown in Fig. 23. The IO324-200K module handled analog input and output functions, while

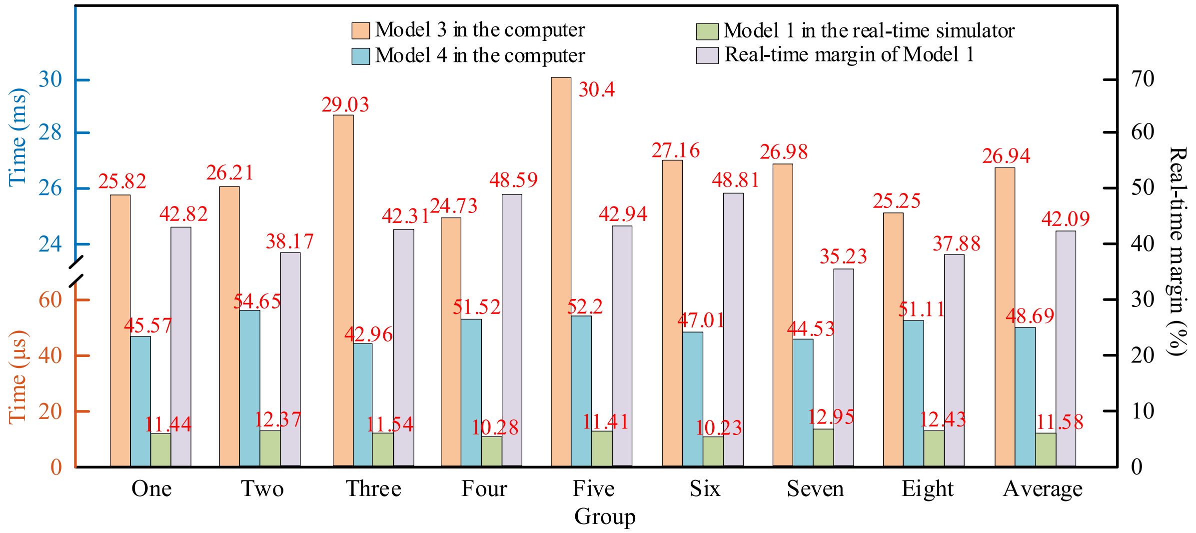

Fig. 20. The average computation time per sampling step of Model 3 and Model 4 in computer, the average computation time per sampling step and the real-time margin of Model 1 in real-time simulator.

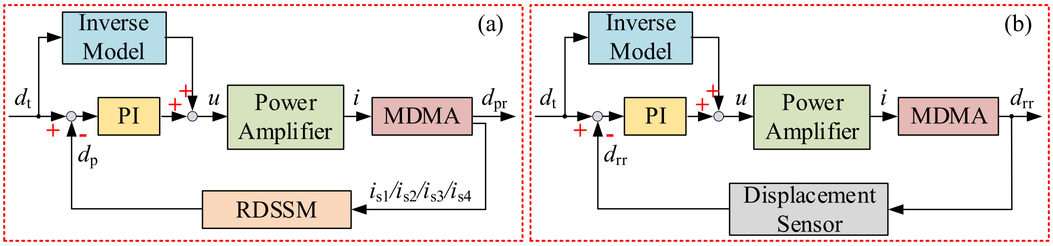

Fig. 21. The architecture and principle of the closed-loop control system. In which, d_t represents the target displacement; d_p represents the predictive displacement of the RDSSM; d_{pr} represents the measured displacement when the predictive displacement of the RDSSM served as the feedback variable; and d_{rr} represents the measured displacement when the displacement measured by the displacement sensor served as the feedback variable.

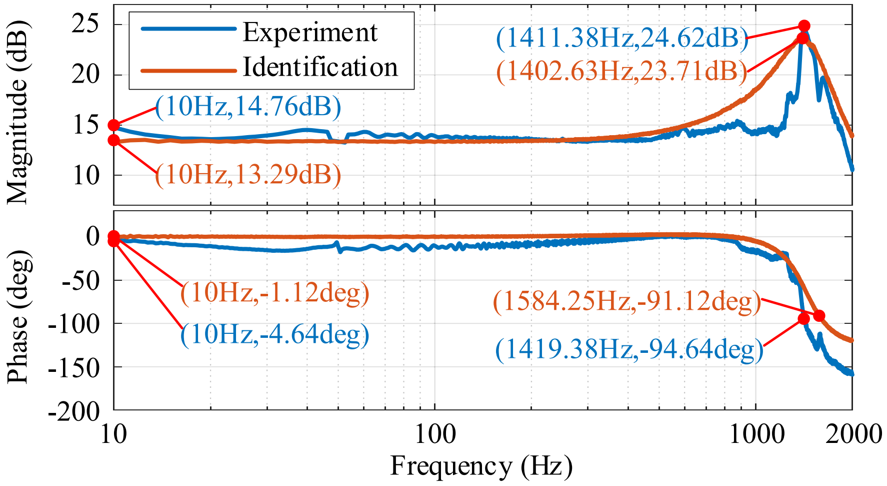

Fig. 22. The frequency response curves of the MDMA prototype and the nominal model.

the pre-treatment module incorporated both the DWT and normalization algorithms. The model was implemented and executed on the real-time simulator, and four experimental trials with different target displacements were conducted using the experimental platform shown in Fig. 12.

Due to the limited robustness of the PI controller, significant control errors occurred were observed in response to variations in the target displacement. Therefore, this study optimized and assigned specific PI controller parameters tailored to each target displacement. The amplitudes and frequencies of the four sinusoidal target displacement signals, along with their respective optimized PI controller parameters, are presented in Table 12.

Fig. 24 illustrates the results of the closed-loop control comparison experiments, with subfigures (a) to (d) corresponding to Groups One to Four, respectively. Analysis of data from all four groups revealed that the curves of d_{rr} and d_{pr} exhibited a noticeable temporal lag relative to those of d_t. Specifically, at frequencies of 400 Hz, 500 Hz, 600 Hz, and 700 Hz, the curves of d_{rr} lag behind those of d_t by 0.7 ms, 0.74 ms, 0.62 ms, and 0.66 ms, respectively. This observed delay was attributed to an inherent 0.4 ms latency in the signal acquisition and conversion process of the capacitive displacement sensor. Notably, this delay could not be compensated by the feedforward controller. Despite this lag, the displacement curves of d_{rr}, d_{pr} and d_p demonstrated a high degree of congruence across all four groups.

Using d_{rr} as the reference baseline, the relative errors of d_{pr} and d_p are represented by the red and green dashed lines in Fig. 24, respectively. Across all groups, the maximum relative error did not exceed 5 μm. Additionally, Fig. 25 presents a comparative analysis of relative error metrics, including maximum error, average error, and root mean square error. The data indicate that Group Three exhibited the highest values for these error metrics, which was attributed to the larger amplitude of d_t within this group. Conversely, the other three groups displayed comparatively lower error magnitudes.

This study further quantified the errors associated with d_{pr} and d_p relative to d_{rr} by calculating the ratio of the mean error to the amplitude of d_{rr}. The computational formula used is provided below, and the corresponding results are summarized in Table 13.

$$\text{Error} = \frac{e_{\text{Average}}}{d_{\text{rrA}}} \times 100\% \tag{26}$$

Where e_{Average} represent the average error, and d_{rrA} represent the amplitude of d_{rr}.

Across the four closed-loop experiments, the deviations of d_{pr} and d_p relative to d_{rr} consistently remained below 7 %. Notably, the maximum error of d_{pr} relative to d_{rr} was 5.05 %, with an average error of 3.76 %, while the maximum error of d_p relative to d_{rr} reached 6.59 %, accompanied by an average error of 4.95 %. These findings indicated that the RDSSM demonstrated high accuracy and could serve as a viable substitute for the displacement sensor within closed-loop control systems, thereby enabling accurate self-sensing, feedback, and control of the inner spool position.

6. Conclusion

In order to explore a non-contact measurement technique for monitoring the inner spool position of the DSFV, this study conducted research on the modeling and experiments of the self-sensing displacement of the high-frequency MDMA. In contrast to previous studies, this study was the first to extend the application of self-sensing displacement technology for magnetostrictive actuators from low-frequency off-line calculations not exceeding 10 Hz to the high-frequency on-line real-time solutions up to 700 Hz, while maintaining comparable modeling accuracy. Although the amplitude of high-frequency self-sensing signals surpassed that of low-frequency signals, which to some extent benefitted signal acquisition and feature extraction, it also imposed more stringent requirements on the computational efficiency, real-time performance and accuracy of the self-sensing displacement model. The closed-loop control experiments using the RDSSM demonstrated precise self-sensing, feedback, and control of the inner spool position, thereby confirming the efficacy and accuracy of self-sensing displacement technology in high-frequency applications. Furthermore, compared to the traditional displacement sensors, the displacement self-sensing system eliminated the need for an additional power supply, thereby reducing energy consumption. The specific conclusions are as follows:

Table 12
The amplitudes and frequencies of the target displacement signals and the PI controller parameters.

Group	One	Two	Three	Four
Amplitude (μm)	24	16	32	20
Frequency (Hz)	400	500	600	700
k_p	0.045	0.045	0.037	0.05
k_i	160	188	130	122

(1) The displacement self-sensing strategy was proposed using four sets of induction coils arranged axially within the MDMA, and based on the energy transfer process, the theoretical model of the self-sensing displacement was established to reveal the intrinsic relationship between the displacement and induced current under the influence of magnetic field. The findings from eight comparative experiments demonstrated that the relative error between the theoretical model and the measurements remained below 8 %, with an average of 5.48 %.

(2) By employing the DWT algorithm and a two-layer MLP network, the RDSSM was proposed to realize the real-time self-sensing of the high-frequency displacement. The proposed RDSSM predicted the self-sensing displacement by the sampled data from four distinct sets of induction coils over five consecutive time intervals. The findings from eight comparative experiments

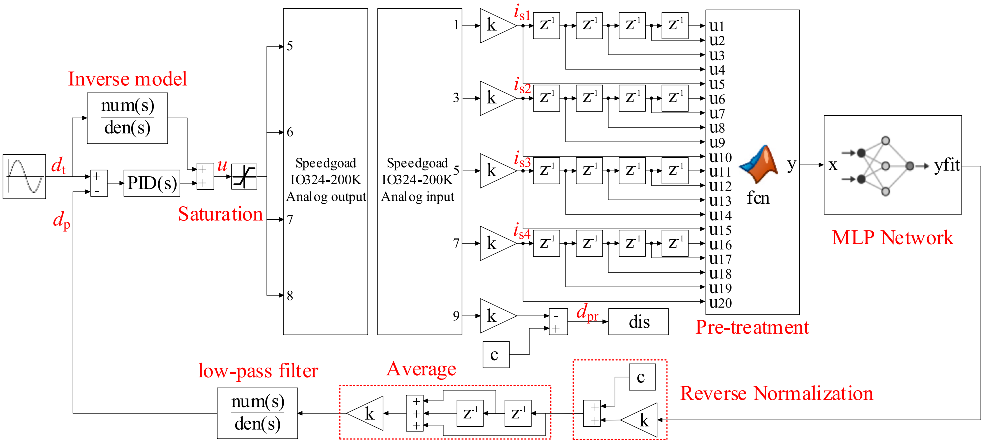

Fig. 23. The Simulink real-time simulation model.

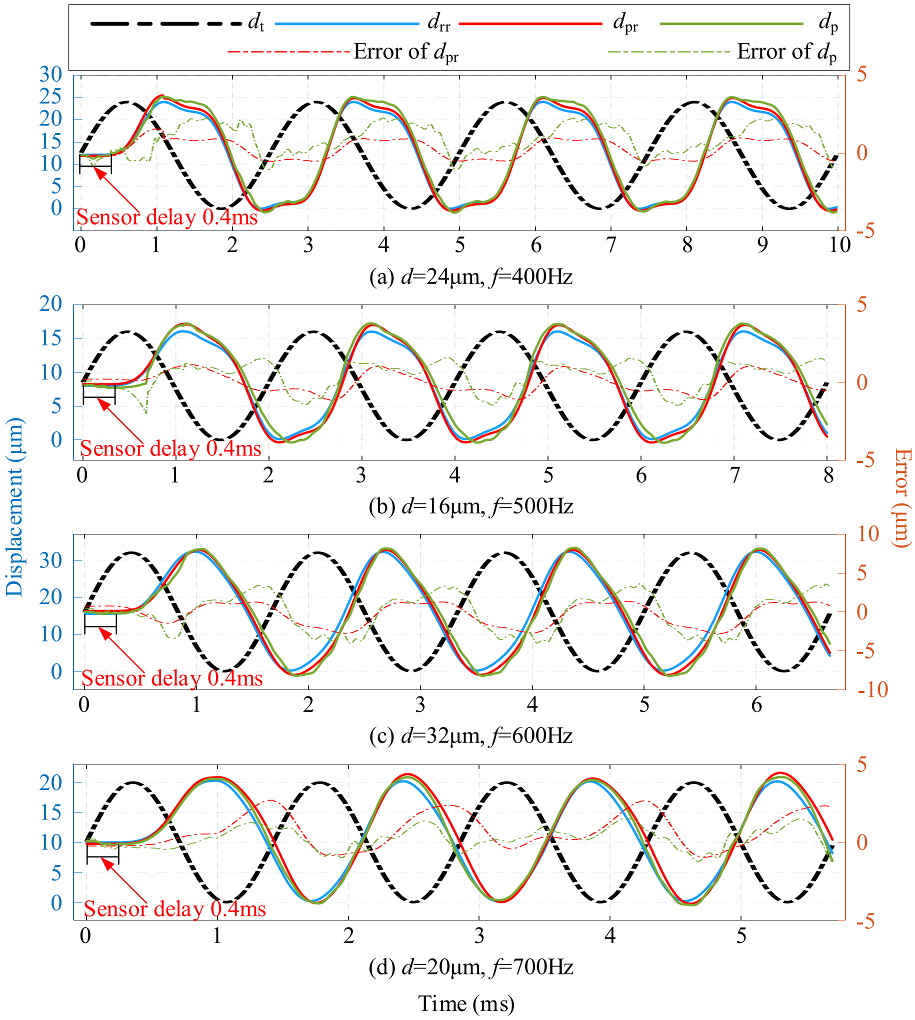

(a) d=24μm, f=400Hz

(b) d=16μm, f=500Hz

(c) d=32μm, f=600Hz

(d) d=20μm, f=700Hz

Fig. 24. The results and errors of the closed-loop control experiments.

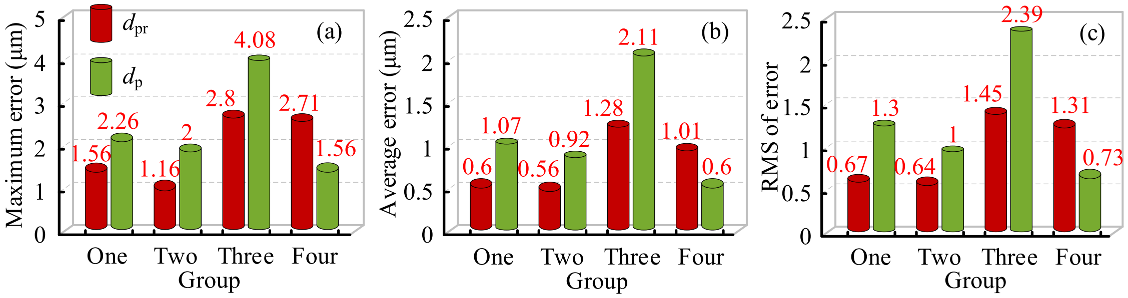

Fig. 25. The specific values of the errors of the closed-loop control experiments.

Table 13
The errors of d_{pr} and d_p.

Group	One	Two	Three	Four	Average
d_{pr}	2.5 %	3.5 %	4 %	5.05 %	3.76 %
d_p	4.46 %	5.75 %	6.59 %	3 %	4.95 %

demonstrated that the relative error between the RDSSM and self-sensing remained below 7 %, with an average of 3.63 %. In addition, the RDSSM demonstrated an average computation time per sampling step of 11.58 μs in the real-time simulator with a sampling frequency of 50 kHz and preserved an average real-time margin of 42.09 %, which afforded a relatively ample temporal allowance for the implementation of simple linear control algorithms.

(3) This study conducted four sets of closed-loop control comparative experiments with varying target displacements. The results indicated that using self-sensing displacement of the RDSSM as the feedback variable, rather than directly measured displacement, resulted in a maximum error of 5.05 % and an average of 3.76 %.

(4) Further studies across varying temperature conditions are necessary to validate the adaptability of the self-sensing model in high temperature conditions. For the theoretical model, accurate analytical formulas for temperature-dependent parameters must be developed to effectively capture the influence of temperature variations on the model. In the case of RDSSM, temperature should be included as an input variable to improve the generalization ability across different temperature conditions.

CRediT authorship contribution statement

Chengyuan Li: Writing – original draft, Software, Methodology, Investigation, Formal analysis. **Long Chen:** Writing – review & editing, Methodology. **Hao Zhang:** Writing – review & editing, Software. **Yuchuan Zhu:** Writing – review & editing, Conceptualization.

Declaration of competing interest

The authors declare that they have no known competing financial interests or personal relationships that could have appeared to influence the work reported in this paper.

Acknowledgements

This work was supported by the National Natural Science Foundation of China (Grant No. 52375059), the Natural Science Foundation of Jiangsu Province (Grant No. BK20251512) and the Postgraduate Research & Practice Innovation Program of Jiangsu Province (Grant No. KYCX25_0599).

Data availability

Data will be made available on request.

References

[1] Shi Y, Lu J, Liu X, Lv G, Liu E, Zheng H. Dynamic characteristics analysis under different flame modes in coaxial staged combustor. Aero Sci Technol 2025;162:110181. https://doi.org/10.1016/j.ast.2025.110181.

[2] Lv G, Liu X, Zhang Z, Li S, Liu E, Zheng H. The effects of premixed pilot-stage on combustion instabilities in stratified swirling flames: a large eddy simulation study. Energy 2023;274:127246. https://doi.org/10.1016/j.energy.2023.127246.

[3] Peng J, Gao L, Yu X, Liu F, Liu B, Cao Z, Wu G, Han M. Combustion oscillation characteristics of a supersonic ethylene jet flame using high-speed planar laser-induced fluorescence and dynamic mode decomposition. Energy 2022;239:122330. https://doi.org/10.1016/j.energy.2021.122330.

[4] Huang Y, Yang V. Dynamics and stability of lean-premixed swirl-stabilized combustion. Prog Energy Combust 2009;35:293–364. https://doi.org/10.1016/j.pecs.2009.01.002.

[5] Tang A, Cai T, Li C, Zhou C, Gao L. Flame visualization and spectral analysis of combustion instability in a premixed methane/air-fueled micro-combustor. Energy 2024;294:130793. https://doi.org/10.1016/j.energy.2024.130793.

[6] Zhao D, Lu Z, Zhao H, Li X, Wang B, Liu P. A review of active control approaches in stabilizing combustion systems in aerospace industry. Prog Aero Sci 2018;97:35–60. https://doi.org/10.1016/j.paerosci.2018.01.002.

[7] Nabae H, Higuchi T. A novel electromagnetic actuator based on displacement amplification mechanism. IEEE-ASME T Mech 2014;20:1607–15. https://doi.org/10.1109/TMECH.2014.2360316.

[8] Guo H, Wang D, Xu J. Research on a high-frequency response direct drive valve system based on voice coil motor. IEEE Trans Power Electron 2012;28:2483–92. https://doi.org/10.1109/TPEL.2012.2213345.

[9] Mohammadi S, Esfandiari A. Magnetostrictive vibration energy harvesting using strain energy method. Energy 2015;81:519–25. https://doi.org/10.1016/j.energy.2014.12.065.

[10] Li A, Kobayashi Y, Hara Y, Otsuka K, Makihara K. Magnetostrictive-based induced current inversion and amplification: semi-active vibration suppression for multiple-degree-of-freedom flexible structures. J Sound Vib 2024;568:118069. https://doi.org/10.1016/j.jsv.2023.118069.

[11] Ghodsi M, Hosseinzadeh N, Özer A, Dizaj HR, Hojjat Y, Varzeghani NG, Sheykholeslami MR, Talebian S, Ghodsi MH, Yahmadi AA. Development of gasoline direct injector using giant magnetostrictive materials. IEEE Trans Ind Appl 2016;53:521–9. https://doi.org/10.1109/TIA.2016.2606591.

[12] Larson JP, Dapino MJ. Reliable, high-frequency miniature valves for smart material electrohydraulic actuators. J Intell Mater Syst Struct 2012;23:805–13. https://doi.org/10.1177/1045389X12438628.

[13] DeLaat J, Breisacher K, Saus J, Paxson D. Active combustion control for aircraft gas turbine engines. In: 36th AIAA/ASME/SAE/ASEE joint propulsion conference and exhibit; 2000, July. p. 3500. https://doi.org/10.2514/6.2000-3500.

[14] Chen L, Zhu Y, Ling J. Development and characteristic analysis of a double spool nested fuel valve. In: 2023 9th international conference on fluid power and mechatronics (FPM). IEEE; 2023, August. p. 1–5. https://doi.org/10.1109/FPM57590.2023.10565525.

[15] Chen L, Zhu Y, Ling J, Zhang M. Development and characteristic investigation of a multidimensional discrete magnetostrictive actuator. IEEE-ASME T Mech 2022;27:2071–9. https://doi.org/10.1109/TMECH.2022.3173619.

[16] Chen L, Zhu Y, Ling J, Zhang M. Temperature dependence modeling and experimental evaluation of a multidimensional discrete magnetostrictive actuator. Appl Therm Eng 2023;230:120736. https://doi.org/10.1016/j.applthermaleng.2023.120736.

[17] Li C, Zhu Y. Semi-physical experimental research for active control of high-frequency combustion oscillation based on dual spool fuel valve. Energy 2025;338:138815. https://doi.org/10.1016/j.energy.2025.138815.

[18] Xie D, Zhang Y, Wu H, Yang Y, Yang B. Experimental study on synchronous detection of output force in a self-sensing giant magnetostrictive actuator. J Phys D Appl Phys 2024;57:395005. https://dx.doi.org/10.1088/1361-6463/ad5c74.

[19] Xie D, Yang Y, Zhang Y, Yang B. Precision positioning based on temperature dependence self-sensing magnetostrictive actuation mechanism. Int J Mech Sci 2024;272:109174. https://doi.org/10.1016/j.ijmecsci.2024.109174.

[20] Chen J, Wang L, Yu J, Sun H, Wang J, Zhang H. Self-sensing model of low-frequency magnetostrictive composites actuator based on Jiles-Atherton theory. Smart Mater Struct 2024;33:055010. https://dx.doi.org/10.1088/1361-665X/ad378a.

[21] Xie D, Yang Y, Yang B. Self-sensing magnetostrictive actuator based on ΔE effect: design, theoretical modeling and experiment. Smart Mater Struct 2022;31:055007. https://dx.doi.org/10.1088/1361-665X/ac5c88.

[22] Apicella V, Clemente CS, Davino D, Leone D, Visone C. Self-sensing estimation of mechanical stress in magnetostrictive actuators. IEEE Trans Magn 2019;55:2500106. https://dx.doi.org/10.1109/TMAG.2018.2873179.

[23] Yang Y, Wang L, Tan J, Zhu X, Zhao B, Jin G, Zhao X, Liu Y. Self-sensing giant magnetostrictive actuator for active vibration isolation. Appl Mech Mater 2017;870:67–72. https://dx.doi.org/10.4028/www.scientific.net/AMM.870.67.

[24] Yan B, Zhang C, Li L, Lv F, Deng S. Conceptual design of self-sensing actuator based on giant magnetostrictive material. In: 2014 17th international conference on electrical machines and systems (ICEMS); 2014. https://dx.doi.org/10.1109/ICEMS.2014.7013762.

[25] Yan B, Zhang C, Li L, Tang Z, Lv F, Yang K. Modelling self-sensing of a magnetostrictive actuator based on a terfenol-D rod. Chin Phys B 2014;23:127504. https://dx.doi.org/10.1088/1674-1056/23/12/127504.

[26] Sun S, Hu T, Zheng G, Ma C. Research on self-sensing signal identification and extraction technology of giant magnetostrictive actuator. Appl Mech Mater 2013;401:1102–5. https://doi.org/10.4028/www.scientific.net/AMM.401-403.1102.

[27] Kuhnen K, Schommer M, Janocha H. Integral feedback control of a self-sensing magnetostrictive actuator. Smart Mater Struct 2007;16:1098. https://doi.org/10.1088/0964-1726/16/4/019.

[28] Kopasakis G. High frequency adaptive instability suppression controls in a liquid-fueled combustor. In: 39th AIAA/ASME/SAE/ASEE joint propulsion conference and exhibit; 2003, July. p. 4491. https://doi.org/10.2514/6.2003-4491.

[29] Mehrpanahi A, Naserabad SN, Ahmadi G. Multi-objective linear regression based optimization of full repowering a single pressure steam power plant. Energy 2019;179:1017–35. https://doi.org/10.1016/j.energy.2019.04.208.

[30] Huo Y, Zhang R, Zhang R, Ren S. Linear calibration models for mass defects of hemispherical resonator. Int J Mech Sci 2025:110644. https://doi.org/10.1016/j.ijmecsci.2025.110644.

[31] Kamali S, Mariani S, Hadianfard MA, Marzani A. Inverse surrogate model for deterministic structural model updating based on random forest regression. Mech Syst Signal Process 2024;215:111416. https://doi.org/10.1016/j.ymssp.2024.111416.

[32] Dong Z, Chen Y, Zhou D, Su J, Han Z, Cao Y, Bao Y, Zhao F, Wang R, Zhao Y, Xu Y. The mean wake model and its novel characteristic parameter of H-rotor VAWTs based on random forest method. Energy 2022;239:122456. https://doi.org/10.1016/j.energy.2021.122456.

[33] Farhan M, Chen TH, Rao A, Shahid MI, Xiao QH, Salam HA, Ma FH. An experimental study of knock analysis of HCNG fueled SI engine by different methods and prediction of knock intensity by particle swarm optimization-support vector machine. Energy 2024;309:133165. https://doi.org/10.1016/j.energy.2024.133165.

[34] Ma Y, Zhang X, Xu M, Xie S. Hybrid model based on Preisach and support vector machine for novel dual-stack piezoelectric actuator. Mech Syst Signal Process 2013;34:156–72. https://doi.org/10.1016/j.ymssp.2012.05.015.

[35] Wen C, Li J, Wang B, Lu G, Xu H. Expertise-guided NOx emission modeling of hybrid vehicle engines via peak-valley-enhanced Gaussian process regression. Energy 2025;322:135166. https://doi.org/10.1016/j.energy.2025.135166.

[36] Zhang H, Li J, Yan M, Miao Y. Optimization of supersonic combustor configuration based on Gaussian process regression and genetic algorithm. Aero Sci Technol 2025;159:109980. https://doi.org/10.1016/j.ast.2025.109980.

[37] Lu X, Wang Y. Surrogate modeling for radiative heat transfer using physics-informed deep neural operator networks. Proc Combust Inst 2024;40:105282. https://doi.org/10.1016/j.proci.2024.105282.

[38] Chen T, Kang Y, Yan P, Yuan Y, Feng H, Wang J, Zhai H, Zha Y, Zhou Y, Tian GY, Wang Y. Supercritical carbon dioxide critical flow model based on a physics-informed neural network. Energy 2024;313:133863. https://doi.org/10.1016/j.energy.2024.133863.

[39] Teng D, Feng Y, Chen J, Lu C. Intelligent vectorial surrogate modeling framework for multi-objective reliability estimation of aerospace engineering structural systems. Chin J Aeronaut 2024;37:156–73. https://doi.org/10.1016/j.cja.2024.06.020.

[40] Chen L, Zhu Y, Ling J, Feng Z. Theoretical modeling and experimental evaluation of a magnetostrictive actuator with radial-nested stacked configuration. Nonlinear Dyn 2022;109(3):1277–93. https://doi.org/10.1007/s11071-022-07494-4.